

CoBiToM Project - II: Evolution of contact binary systems close to the orbital period cut-off

G. A. Loukaidou,^{1*} K. D. Gazeas,¹ S. Palafouta,¹ D. Athanasopoulos,¹ S. Zola,^{2,3}
A. Liakos,⁴ P. G. Niarchos,¹ P. Hakala,⁵ A. Essam⁶ and D. Hatzidimitriou¹

¹ Section of Astrophysics, Astronomy and Mechanics, Department of Physics, National and Kapodistrian University of Athens, GR-15784 Zografos, Athens, Greece

² Astronomical Observatory, Jagiellonian University, ul. Orła 171, PL-30-244 Krakow, Poland

³ Mt. Suhora Observatory, Pedagogical University, ul. Podchorążych 2, PL-30-084 Krakow, Poland

⁴ IAASARS, National Observatory of Athens, GR-15236 Penteli, Athens, Greece

⁵ Finnish Centre for Astronomy with ESO (FINCA), Quantum, University of Turku, FI-20014, Turku, Finland

⁶ Department of Astronomy, National Research Institute of Astronomy and Geophysics (NRIAG), Helwan, Cairo 11421, Egypt

Accepted XXX. Received YYY; in original form ZZZ

ABSTRACT

Ultra-short orbital period contact binaries ($P_{orb} < 0.26$ d) host some of the smallest and least massive stars. These systems are faint and rare, and it is believed that they have reached a contact configuration after several Gyrs of evolution via angular momentum loss, mass transfer and mass loss through stellar wind processes. This study is conducted in the frame of *Contact Binaries Towards Merging (CoBiToM) Project* and presents the results from light curve and orbital analysis of 30 ultra-short orbital period contact binaries, with the aim to investigate the possibility of them being red nova progenitors, eventually producing merger events. Approximately half of the systems exhibit orbital period modulations, as a result of mass transfer or mass loss processes. Although they are in contact, their fill-out factor is low (less than 30 per cent), while their mass ratio is larger than the one in longer period contact binaries. The present study investigates the orbital stability of these systems and examines their physical and orbital parameters in comparison to those of the entire sample of known and well-studied contact binaries, based on combined spectroscopic and photometric analysis. It is found that ultra-short orbital period contact binaries have very stable orbits, while very often additional components are gravitationally bound in wide orbits around the central binary system. We confirmed that the evolution of such systems is very slow, which explains why the components of ultra-short orbital period systems are still Main Sequence stars after several Gyrs of evolution.

Key words: binaries: eclipsing – binaries (including multiple): close – stars: fundamental parameters – stars: evolution – stars: low mass.

1 INTRODUCTION

The present work is a continuation of *CoBiToM Project I - Contact Binaries Towards Merging* (Gazeas et al. 2021b), which aims to investigate the stellar merging processes by utilising contact binary systems as probes of coalescence events. It follows the same rationale and scientific approach for deriving the physical parameters of the binary components. The present study focuses on contact binary systems with ultra-short orbital periods, with the main goal being the determination of their physical and orbital characteristics, providing indications about the evolution of the binary before merging.

Contact binary systems consist of Main Sequence (MS) stars,

possibly formed from an initial detached configuration, after gradual angular momentum loss, which leads to orbital shrinking (Stępień & Gazeas 2012). The stellar evolution of the components of a contact binary system is significantly different from that of single stars. The evolution is controlled by mass loss and hence angular momentum loss from the system, along with mass transfer between the components (e.g. Yakut & Eggleton 2005; Stępień 2006), gradually brings the components closer to each other. The question of whether there is an evolutionary sequence among different types of contact binary systems is still open. It is clear that energy transfer between the components in the contact configuration alters their evolution and therefore their parameters (such as mass, radius and temperature) depend on it. The high proximity between the components and the mass transfer affects the gravity vs

* E-mail: georgialouk@phys.uoa.gr

radiation equilibrium. Consequently, components of close contact binary systems differ from their single stars counterparts.

The continuous monitoring of the absolute physical and orbital parameters of the binary components in such systems, as well as their secular changes, provide the tools for understanding stellar evolution, under this environment. These parameters are constrained by Roche geometry, as the contact configuration has to be preserved, restricting the radius of the components, the orbital separation, and therefore the mass and orbital period. Correlation between orbital and physical parameters show that these parameters are highly correlated with each other, as a result of a common evolution scheme (Hilditch et al. 1988; Gazeas & Niarchos 2006).

The orbital period distribution of contact binary systems ranges between 0.22 and 1.1 d, while Rucinski (1992) noticed a sharp period cut-off limit at a value of ~ 0.22 d. More recent observational evidence has indicated that the period cut-off could be even shorter than 0.22 d. Davenport et al. (2013) presented the system SDSS J001641-000925 with an orbital period of 0.19856 d. Nefs et al. (2012) detected nine eclipsing binary candidates with orbital period of less than 0.22 d (ranging between 0.15-0.21 d) in the Wide-Field Camera (WFCAM) Transit Survey, five of which were classified as contact binaries. Drake et al. (2014b) identified 231 contact binaries with an orbital period below the cut-off limit, utilizing data from the Catalina Sky Survey (CSS). Zhang & Qian (2020) used a combination of observational and theoretical arguments to suggest a new orbital period cut-off limit, at approximately 0.15 d.

There have been several attempts to explain the existence of the observed orbital period cut-off. First, Rucinski (1993) proposed a model, where stars with low surface temperature become fully convective. This ultimately constrains the range of orbital parameters of contact binaries and therefore a random combination of stars cannot always be placed into a contact configuration. An alternative approach was proposed by Stępień (2006); Stępień & Gazeas (2012), who conducted detailed calculations and showed that the orbital period cut-off in low-mass contact binaries can be explained by the very large dynamical evolution timescale. The angular momentum and mass loss rate in these systems is so slow, that several billion years are needed for a close binary to reach a contact configuration from an initially detached one, which shall slowly present a period decrease. For example, for an equal mass component detached binary with an initial mass of $1 M_{\odot}$, 7.5 Gyrs are approximately needed in order to start their contact phase. However, when the initial mass is $0.7 M_{\odot}$, then more than 13 Gyrs are needed to reach a contact configuration and gradually decrease the orbital period to the values we observe today. On the other hand, Jiang et al. (2012) suggested that the period cut-off is a result of the instability of the mass transfer that occurs when the primaries of the initially detached binaries fill their Roche lobes. They suggested that when the initial mass of the primary is lower than a certain value (approximately $0.63 M_{\odot}$), mass transfer occurs as soon as the primary component inflates and reaches its Roche lobe limit. The system is then dynamically unstable and quickly becomes a common envelope binary, ultimately leading to a coalescence event. Only stars with masses above this value, may form long-lived contact binaries with an orbital period longer than 0.22 d.

The aforementioned possible explanations of the cut-off limit are still under debate and observational constrains are necessary. This is the main goal of the present paper. The construction of accurate models and the correlation among orbital and physical parameters of ultra-short period contact binaries is the best way to test these theories and explain the observed period cut-off limit. The key

to achieve this goal is to have reliable results and improve significantly the accuracy of the determination of the physical parameters of the components of binary systems, as well as reduce the control systematics. This can be achieved by acquiring data with the same instrumentation, reaching sufficient signal to noise ratio and using the same well defined methodology and data reduction procedure. These criteria are fulfilled in the *CoBiToM Project* (Gazeas et al. 2021b), providing as accurate as possible solutions leading to important information about the nature of these systems and their environment.

Thousands of contact binaries have been detected in recent major surveys and catalogues, such as AAVSO (Watson et al. 2006), ASAS (Paczynski et al. 2006), ASAS-SN (Jayasinghe et al. 2019), CoRoT (Deleuil et al. 2018), CSS (Drake et al. 2014b), GCVS (Samus et al. 2018), Kepler (Kirk et al. 2016), LAMOST (Qian et al. 2020), OGLE (Soszyński et al. 2016), SWASP (Lohr et al. 2013), WISE (Petrosky et al. 2021), and ZTF (Chen et al. 2020). The percentage of ultra-short contact binaries (with $P < 0.26$ d) among contact binaries in these surveys ranges between 1.8 and 13.8 per cent, with an average value of 6.6 per cent. These values depend on the detection and classification methods applied and vetting of false positives (e.g. pulsating stars with short periods, i.e. Rucinski 2002; Drake et al. 2014a). Hence, in the present study, a sample of 30 ultra-short orbital period contact binary systems ($P_{orb} < 0.26$ d) is presented and examined under the scope of their physical and orbital properties. All systems were homogeneously observed and analysed, and only a few of them have been previously investigated in other studies using their light curves, $O-C$ diagrams and physical parameters at the same time. Therefore, we present the analysis of recent and unpublished multi-band photometric observations with well known and accurate techniques, combined with all the available spectroscopic data.

The paper is organized as follows: In Section 2 we describe the selection of ultra-short contact binaries, leading to a sample of 30 systems, as well as their new photometric observations. Section 3 presents the data analysis procedure used for obtaining the light curve models and interpreting the resulted uncertainties. The physical parameters of the targets are presented in Section 4, while an extended orbital period analysis is performed in Section 5. Finally, Section 6 includes an overview of the physical properties of the systems in the sample, followed by a discussion on their evolution status and dynamical stability.

2 TARGET SELECTION AND DATA ACQUISITION

2.1 Target Selection

Our sample of ultra-short contact binaries were selected from the SWASP catalogue (Norton et al. 2011). The main criteria used to include a target in the working sample were a contact binary classification and an orbital period shorter than 0.26 d. Additionally, targets should have multi epoch data covering approximately 3-7 yr, thus ensuring a sufficient number of times of minimum light and hence a wide time span in the orbital period analysis through $O - C$ diagrams. Finally, all selected systems should be brighter than 16 mag due to the observational constraints of the collaborating observatories in the *CoBiToM Project*. A sub-sample of our investigation, containing 30 ultra-short orbital period systems, will be shown in the present paper, as the rest of the sample will be discussed in forthcoming studies.

In Table 1 the IDs of our sample, along with the ephemerides

and a detailed observing log are provided. During the definition of our sample, we have noticed in some cases that there was a confusion concerning the exact celestial coordinates, the amplitude of light variation and sometimes the orbital period in the literature. Close inspection revealed that seven of the selected 30 systems had wrong IDs in the literature, an issue that was also noted in some cases by Zhang et al. (2014) and Koen et al. (2016). In Table 1 and throughout the paper, we use the updated IDs.

The amplitude of variability is also noticed to be larger when high angular resolution photometry is performed. For example, the eclipse depth reported by Norton et al. (2011) using the small aperture SWASP cameras was found to be significantly smaller in some cases, compared to our follow-up observations with much larger aperture telescopes. This issue is expected, when low-resolution instruments are used, when seeing conditions are poor or even when smearing effects play significant role in the observations. Low spatial resolution results in light contamination by close companions and the observed light curve (and therefore the eclipse depth) appears shallower.

2.2 Observations

Publicly available photometric data for the targets under study provided a sufficient number of eclipse timings spanning over an adequate period of time. However, this is not long enough for the purpose of a detailed orbital period modulation analysis, as seen through the $O - C$ diagrams. In addition, photometric accuracy by small aperture telescopes is rather poor, limiting significantly the quality of the resulting models and the calculation of the absolute physical and orbital parameters. Therefore, we revisited our sample, by performing follow-up observations with the University of Athens Observatory (UOAO), and the telescopes of the National Observatory of Athens (NOA) at Helmos and Kryoneri Astronomical Stations. An analytical description of the astronomical equipment in each facility is described in the first paper of the series (Gazeas et al. 2021b). Supplementary data of the southern targets were also utilized in this study for the systems that can not be observed from the northern latitudes. These data were collected with the 1 m telescope at South African Astronomical Observatory (SAAO), following the observing strategy described by Koen et al. (2016).

The aim of the observations was the acquisition of multi-band photometric data (the filter set is mentioned in the seventh column in Table 1) for all targets under study. Differential aperture photometry was performed in all cases. In order to collect uniform photometric data and construct the phased light curves, all observations were obtained using only one instrumental setup for each target, in order to avoid any systematic effects due to instrumental cross calibration or filter mismatch.

For the purpose of extending the timescale of the $O - C$ diagrams, recent supplementary observations around the eclipse phase have been conducted in most targets in order to provide additional epochs. These data were not used in the light curve modeling process. Our goal during the entire observing period was to obtain a complete light curve within a few days, in order to minimize the effect of any intrinsic variability (e.g. magnetic activity). The timescale of any intrinsic variability is usually significantly longer than the duration of our observations, since the orbital period of all systems is short enough to be covered within one night. Therefore, the light curves modeled in this paper represent a ‘snapshot’ of a system’s photometric behaviour over the duration of observations. A detailed observing log is presented in Table 1 and includes the

observing dates, the total number of nights dedicated to each target and the observing telescope.

3 DATA ANALYSIS AND LIGHT CURVE MODELING

The data were reduced following standard procedures of aperture photometry and calibration. Differential photometry was subsequently performed, with a photometric accuracy between 5–10 mmag. Times of minimum light were used to derive precise ephemerides for the systems as described in section 3.1. The light curves were period folded and then modelled as described in section 3.3. This modeling requires the effective temperature of the primary component T_1 (the component that is eclipsed at phase 0) as a prior, as described in section 3.2.

3.1 Times of minimum light and linear ephemerides

Photometric times of minimum light were collected within the framework of the *CoBiToM Project* over the last decades. The times of minimum light were calculated using the method of Kwee & van Woerden (Kwee & van Woerden 1956). From these timings, the linear astronomical ephemerides were calculated. Using the derived orbital period, the light curves were folded to show one single orbital period. Table 1 lists the linear ephemerides of all systems along with their uncertainties.

Additional times of minimum light were also extracted from all the available online time-series photometric data (SWASP, ASAS-SN, ASAS, CSS, and NSVS surveys). In all cases, where the retrieved data are sparse (i.e. data from the catalogues NSVS, ASAS, ASAS-SN and CSS), we followed the same procedure of folding the data into “local” phase diagrams, according to the methodology described by Li et al. (2020). Times of minimum light of some targets were also found in online minima databases^{1 2}.

Early studies on individual targets provided an additional source of eclipse timing information. We collected times of minimum light from the following publications: Li et al. (2020); peng Lu et al. (2020); Fang et al. (2019); Zasche et al. (2019); Kjurkchieva et al. (2018); Haroon et al. (2018); Loukaidou & Gazeas (2018); Darwish et al. (2017); Koen et al. (2016); Djurašević et al. (2016); Saad et al. (2016); Dimitrov & Kjurkchieva (2015); Liu et al. (2015); Koo et al. (2014); Elkhateeb et al. (2014); Zhang et al. (2014); Terrell & Gross (2014).

Utilising the information from all the above sources, $O - C$ diagrams for each target of our sample were constructed, following the procedure described in Section 5.

3.2 Temperature information and spectroscopy

The effective temperature T_1 in each system was determined from $B - V$ and $g - i$ color indices, using the following procedure: We calculated T_{BV} as the temperature based on the $B - V$ color index, provided by AAVSO Photometric All Sky Survey (APASS) DR9; (Henden et al. 2016), following the conversion provided by Pecauc & Mamajek (2013). Also T_{gi} is the calculated temperature based on the $g - i$ color index (also provided by APASS DR9), following the conversion provided by Covey et al. (2007). Both $B - V$

¹ <http://var2.astro.cz/ocgate/>

² http://www.oa.uj.edu.pl/ktt/krttk_dn.html

Table 1. Targets observed with their linear ephemerides for phasing the observations. The standard errors for each value are expressed in parentheses, in units of last decimal digit quoted. The last three columns provide an observation log for all targets with the observing period, the number of data collecting nights and the observing site.

System ID	GCVS ID	T_0 (HJD)	P_{orb} (d)	Observing Season	Nights	Filters	Site*
1SWASP J030749.87-365201.7	BL For	2457010.41088(24)	0.2266707(4)	Dec 2014	1	BVRI	SAAO
1SWASP J040615.79-425002.3	AQ Hor	2457013.33073(44)	0.22233739(3)	Dec 2014	1	BVRI	SAAO
1SWASP J044132.96+440613.7	V1110 Her	2458039.60234(18)	0.2281521(1)	Sep 2017 - Apr 2021	4+1	BVRI	Helmos+UOAO
1SWASP J050904.45-074144.4	OV Eri	2457639.56377(25)	0.2295749(3)	Dec 2014 - Apr 2021	45+1	BVRI	SAAO+UOAO
1SWASP J052926.88+461147.5	V840 Aur	2458769.62318(21)	0.2266426(2)	Oct 2018 - Apr 2021	3+1	BVRI	Helmos+UOAO
1SWASP J055416.98+442534.0	V853 Aur	2456353.38170(33)	0.21849667(2)	Feb 2013 - Apr 2021	8	BVRI	UOAO
1SWASP J080150.03+471433.8	LX Lyn	2456778.35833(24)	0.21751919(3)	Apr 2014 - Apr 2021	8	BVRI	Kryoneri
1SWASP J092328.76+435044.8	-	2457826.56109(21)	0.2348857(1)	Mar 2017 - Apr 2021	16	BVRI	UOAO
1SWASP J092754.99-391053.4	CO Ant	2456765.37391(28)	0.22534530(4)	Apr 2014	1	UBVR	SAAO
1SWASP J093010.78+533859.5	V442 UMa	2456329.63930(20)	0.22771395(6)	Jan 2013 - Apr 2021	15	BVRI	UOAO
1SWASP J114929.22-423049.0	V1410 Cen	2456758.28401(22)	0.2273081(2)	Apr 2014	1	BVRI	SAAO
1SWASP J121906.35-240056.9	AE Crv	2456768.38662(20)	0.22636763(3)	Apr 2014 - Apr 2021	1+1	BVRI	SAAO+UOAO
1SWASP J133105.91+121538.0	-	2456347.55370(15)	0.21801190(2)	Feb 2013 - Apr 2021	9	BVRI	UOAO
1SWASP J150822.80-054236.9	-	2456352.62854(40)	0.26006086(5)	Feb 2013 - Apr 2021	12	BVRI	UOAO
2MASS J15165453+0048263	V640 Ser	2457956.31802(43)	0.2107323(1)	Apr 2014 - Apr 2021	14+1	UBVR	SAAO+UOAO
1SWASP J161335.80-284722.2	V1677 Sco	2456877.30927(11)	0.2297735(1)	Aug 2014	1	BVRI	SAAO
1SWASP J170240.07+151123.5	-	2457596.41084(18)	0.2614691(3)	Jul 2016 - Apr 2021	29	BVRI	UOAO
1SWASP J173003.21+344509.4	V1498 Her	2456832.36569(49)	0.2237088(1)	Jun 2014 - Apr 2021	4+1	BVRI	Kryoneri+UOAO
1SWASP J173828.46+111150.2	-	2457568.55989(8)	0.2493487(3)	Aug 2014 - Apr 2021	27+1	BVRI	SAAO+UOAO
1SWASP J174310.98+432709.6	V1067 Her	2456778.49931(44)	0.2581081(1)	Apr 2014 - Apr 2021	9+1	BVRI	Kryoneri+UOAO
1SWASP J180947.64+490255.0	V1104 Her	2457629.48307(12)	0.2278766(1)	Jul 2016 - Apr 2021	40	BVRI	UOAO
1SWASP J195900.31-252723.1	-	2456881.33791(38)	0.2381397(2)	Aug 2014 - Apr 2021	1+1	BVRI	SAAO+UOAO
2MASS J21031997+0209339	V496 Aqr	2457946.53396(43)	0.2285901(5)	Sep 2015 - Apr 2021	1+18	BVRI	SAAO+UOAO
2MASS J21042404+0731381	-	2457656.36702(61)	0.2090908(2)	Sep 2015 - May 2021	18+2+1	BVRI	SAAO+Helmos+UOAO
1SWASP J212454.61+203030.8	-	2457271.48793(30)	0.2278308(2)	Sep 2015 - Apr 2021	1+1	BVRI	SAAO+UOAO
1SWASP J212808.86+151622.0	V694 Peg	2458014.28967(9)	0.22484157(9)	Sep 2017 - Apr 2021	1+1	BVRI	Helmos+UOAO
1SWASP J220734.47+265528.6	V729 Peg	2457257.38289(14)	0.2312352(2)	Sep 2014 - Apr 2021	19+2	BVRI	Helmos+UOAO
1SWASP J221058.82+251123.4	V732 Peg	2458012.38783(26)	0.21372960(5)	Sep 2017 - Apr 2021	1+1	BVRI	Helmos+UOAO
1SWASP J224747.20-351849.3	AS PsA	2457279.30511(29)	0.2182159(1)	Sep 2015	1	BVRI	SAAO
1SWASP J232610.13-294146.6	DU Scl	2457274.54580(18)	0.2301173(4)	Sep 2015	1	BVRI	SAAO

(*): UOAO: University of Athens Observatory, Kryoneri: Kryoneri Observatory of National Observatory of Athens

Helmos: Helmos Observatory of National Observatory of Athens, SAAO: South African Astronomical Observatory

and $g-i$ color indices were corrected for reddening, using the extinction tables by [Schlafly & Finkbeiner \(2011\)](#), which are based on the IRAS ³ photometric database. Effective temperature based on the infrared passbands (JHK) and their color indices were not sensitive enough in the range of interest (4000-5000 K), as the $B-V$ and $g-i$ are, and hence they were not included in our approach. Additional spectroscopic data were retrieved from the literature ([Koen et al. 2016](#); [Dimitrov & Kjurkchieva 2015](#); [Lohr et al. 2015a, 2014](#); [Drake et al. 2014b](#)) for 11 systems of our sample, providing independent estimates of the effective temperature T_1 of the primary component.

Table 2 lists in the seventh and eight column the temperature values T_{BV} and T_{gi} obtained by photometric color indices and in the ninth column mentions the spectroscopic temperature T_{sp} . The rounded average (T_m) in the last column was assigned as the effective temperature of the primary component in each system, as it is needed for a prior value in the modeling process. It was calculated by averaging the photometric values in columns T_{BV} and T_{gi} and rounding the value within 50 K, in order to match the closest spectral type. The uncertainty on temperature determination with this method is estimated to be approximately 200 K. For very few cases, the photometric interpretation of the temperature deviated larger than the error. This occurs, due to the possibly spurious reddening determination, that can affect the temperature estimation

and cause large uncertainty. As it can be seen from Table 2, the T_{sp} values are within the error range of our final effective temperature, except for the cases of 1SWASP J050904.45-074144.4 and 1SWASP J150822.80-054236.9, where larger deviations are noted. This fact might be due to the low resolution spectra that were taken in these publications or due to the large uncertainty in reddening determination.

[Casagrande et al. \(2020\)](#) developed a method for determining the effective temperature of single Main Sequence stars using the Gaia color indices, metallicities and limb darkening coefficients. It is known that the majority of contact binaries (about 93 per cent, according to [de Jong et al. \(2010\)](#); and 96 per cent, according to [Aumer & Binney \(2009\)](#), respectively) are solar-metallicity objects, which are spread over the thin Galactic disk. Therefore solar metallicity is a plausible assumption to describe the current sample, a fact that is also confirmed spectroscopically by [Rucinski et al. \(2013\)](#). Consequently, by assuming solar metallicity $[Fe/H] \sim 0$ for our sample and surface gravity coefficient $\log g \sim 4$ for dwarf stars, it was found that the majority of the primary temperature values were within the error range of our approximation, confirming our initial hypothesis for the temperature determination and the metallicity of our sample.

Table 2 also includes the apparent brightness decrease (depth in light curve) during the primary and secondary eclipses, as well as the parallax, distance and absolute magnitude information as derived from Gaia DR2 ([Gaia Collaboration et al. 2018](#)). Taking into

³ <https://irsa.ipac.caltech.edu/applications/DUST/>

Table 2. Astrometric and photometric parameters for the studied systems. The columns include parallax, distance, absolute magnitude in V filter and photometric depth in both eclipses, as well as the temperature values derived from photometric color index and spectroscopic observations. The adopted temperature for the modeling process is T_m .

System ID	Parallax (mas)	d (pc)	M_V (mag)	min_I (mag)	min_{II} (mag)	T_{BV} (K)	T_{gi} (K)	T_{spec} (K)	T_m (K)
1SWASP J030749.87-365201.7	1.82 ± 0.02	550 ± 6	6.08 ± 0.06	0.78	0.64	4797	4591	-	4700
1SWASP J040615.79-425002.3	2.59 ± 0.02	387 ± 3	6.18 ± 0.03	0.62	0.56	4865	4952	5040 ^a	4900
1SWASP J044132.96+440613.7	3.10 ± 0.07	323 ± 7	3.74 ± 0.11	0.95	0.78	5183	5565	-	5350
1SWASP J050904.45-074144.4	3.87 ± 0.02	258 ± 1	6.00 ± 0.15	0.71	0.61	5030	5002	5340 ^a	5000
1SWASP J052926.88+461147.5	1.86 ± 0.04	538 ± 13	4.81 ± 0.12	0.69	0.59	5375	5425	-	5400
1SWASP J055416.98+442534.0	4.94 ± 0.03	203 ± 1	5.48 ± 0.20	0.44	0.42	5189	5286	-	5250
1SWASP J080150.03+471433.8	3.79 ± 0.03	264 ± 2	6.12 ± 0.03	0.71	0.69	4650	4656	4690 ^b	4650
1SWASP J092328.76+435044.8	-	-	-	0.60	0.62	5619	5946	-	5800
1SWASP J092754.99-391053.4	6.12 ± 0.03	163 ± 1	5.10 ± 0.02	0.50	0.42	5324	5469	-	5400
1SWASP J093010.78+533859.5	14.29 ± 0.06	70.0 ± 0.3	6.72 ± 0.08	0.18	0.17	4884	4347	4700 ^c	4700
1SWASP J114929.22-423049.0	4.87 ± 0.02	205 ± 1	7.29 ± 0.04	0.65	0.53	4194	4132	-	4150
1SWASP J121906.35-240056.9	2.13 ± 0.04	470 ± 8	6.63 ± 0.08	0.61	0.51	4656	4675	-	4650
1SWASP J133105.91+121538.0	14.00 ± 0.07	71.4 ± 0.4	6.33 ± 0.03	0.71	0.54	5143	5050	-	5150
1SWASP J150822.80-054236.9	4.30 ± 0.04	232 ± 2	5.40 ± 0.05	0.80	0.71	5202	5115	4500 ^d	5150
2MASS J15165453+0048263	2.58 ± 0.04	388 ± 6	5.89 ± 0.08	0.58	0.49	5910	6417	-	6150
1SWASP J161335.80-284722.2	8.62 ± 0.04	116 ± 1	6.66 ± 0.02	0.81	0.61	4661	4455	-	4550
1SWASP J170240.07+151123.5	2.61 ± 0.02	382 ± 4	5.35 ± 0.05	0.70	0.61	4885	5090	-	5000
1SWASP J173003.21+344509.4	2.89 ± 0.01	347 ± 2	6.00 ± 0.03	0.36	0.30	4838	4570	-	4700
1SWASP J173828.46+111150.2	-	-	-	0.41	0.33	5248	5275	4940 – 5280 ^a	5250
1SWASP J174310.98+432709.6	3.21 ± 0.02	311 ± 2	5.95 ± 0.03	0.70	0.52	5230	5353	-	5300
1SWASP J180947.64+490255.0	5.40 ± 0.01	185 ± 1	7.02 ± 0.01	1.13	0.75	4083	4049	-	4050
1SWASP J195900.31-252723.1	-	-	-	0.72	0.70	5064	5752	-	5400
2MASS J21031997+0209339	2.07 ± 0.05	483 ± 11	6.65 ± 0.12	1.00	0.79	4647	4220	4450 ^a	4400
2MASS J21042404+0731381	1.98 ± 0.07	505 ± 18	5.14 ± 0.20	0.55	0.49	4788	4865	4450 – 5040 ^a	4800
1SWASP J212454.61+203030.8	-	-	-	0.64	0.56	5093	5359	-	5250
1SWASP J212808.86+151622.0	2.53 ± 0.05	395 ± 7	6.29 ± 0.09	0.67	0.52	4621	4727	4450 – 4840 ^a	4700
1SWASP J220734.47+265528.6	1.65 ± 0.03	607 ± 12	5.14 ± 0.10	0.44	0.42	4933	4850	-	4900
1SWASP J221058.82+251123.4	-	-	-	0.66	0.51	4968	4937	-	4950
1SWASP J224747.20-351849.3	2.97 ± 0.02	337 ± 3	6.21 ± 0.04	0.20	0.15	4369	4267	4450 – 4620 ^a	4300
1SWASP J232610.13-294146.6	4.04 ± 0.04	248 ± 3	6.55 ± 0.05	0.60	0.58	4820	4855	4450 – 4840 ^a	4850

Median temperature in the last column is accounted for error approximately of 200 K

(a):Koen et al. (2016), (b):Dimitrov & Kjurkchieva (2015), (c):Lohr et al. (2015a), (d):Lohr et al. (2014)

account the high precision astrometric observations by Gaia satellite for 25 targets of our sample, the distance is accurately determined. It is found that the current sample consists of the nearest binaries in our solar vicinity, all within a radius of ~ 600 pc.

3.3 Light curve modeling

We used the Wilson-Devinney (W-D) code (Wilson 1979, 1990) appended with the Monte Carlo (MC) algorithm as the search procedure, as described in detail in Zola et al. (2004); Gazeas et al. (2021a). We took advantage of the fact that the applied method does not require initial values for the free parameters. Instead, it searches for the best solution within given ranges. We determined the uncertainties of the free parameters using χ^2 minimization according to the method described in Numerical Recipes in Fortran (Press et al. 1996).

Performing the light curve modeling, the albedo and gravity darkening coefficients are fixed at their theoretical values of $A = 0.5$ and $g = 0.32$, respectively (Lucy 1967; Ruciński 1969), since all binary members of the studied systems are low temperature stars ($T < 6500$ K) with convective envelopes. The limb darkening coefficients are taken from the tables of Claret & Bloemen (2011), according to the effective temperature of the components and the filters used.

The parameters which are considered free are: the inclination

(i), the phase shift, the effective temperature of the secondary component (T_2), the gravitational potential ($\Omega_{1,2}$), the luminosity of the primary (L_1), the third light (l_3) and the mass ratio (q). The relative luminosity of the secondary star (L_2) is not a free parameter, because the IPB control parameter was set to 0. In that case, L_2 is computed from geometrical parameters, the luminosity of the primary component, temperature values (T_1 and T_2) and the black body radiation law.

Cool photospheric spots had to be introduced when the light curves showed obvious asymmetries, different maximum brightness levels in the light curves, which are expressed as the O'Connell effect (O'Connell 1951). Light curve asymmetries are exhibited in 19 out of 30 studied systems. In the cases that a cool spot was imposed, four additional parameters were added, in order to describe its location (latitude and longitude), size and temperature factor. It was found that in all cases a single spot was sufficient to explain the observed asymmetry. Large size photospheric spots are introduced, in order to explain asymmetries in light curves of some systems. These are not necessarily single large spots, but could be rather an extended spotted area covered with smaller spots. It is expected that when introducing spots in a solution, the code results in a better fit with smaller residuals, as the degrees of freedom increase. However, the non-uniqueness of a spotted solution is a well known issue in stellar modeling, thus the number of spots is kept to a minimum and spots were added only to explain the observed asymmetries. The third light (l_3) parameter was also adjusted for

systems which have confirmed or proposed additional companions (e.g. based on the $O-C$ diagram or on spectroscopic observations).

An additional check on our modeling results was made for the systems 1SWASP J093010.78+533859.5 and 1SWASP J150822.80-054236.9, which were also studied previously by Lohr et al. (2015a) and Lohr et al. (2014), respectively. These two systems were observed spectroscopically and their mass ratio is determined to be $q_{sp} = 0.397 \pm 0.006$ and $q_{sp} = 0.510 \pm 0.015$, respectively. Computations with the MC code converged to the photometric mass ratio, which was found to be $q_{ph} = 0.415 \pm 0.007$ and $q_{ph} = 0.578 \pm 0.032$, respectively. These values agree within 5 per cent for the totally eclipsing system 1SWASP J093010.78+533859.5 and 13 per cent for the partial eclipsing system 1SWASP J150822.80-054236.9. This gives confidence about the reliability of the mass ratio determination for other systems in the sample in the present study. It is also noted that for nine systems (about 30 per cent of the total sample) that show total eclipses, the photometric determination of the mass ratio is known to be accurately determined (Pribulla et al. 2003; Terrell & Wilson 2005).

The resulting models provide the physical and geometrical parameters of the systems, as given in Tables A1 - A6, together with their 2σ uncertainties. These models are shown together with the observed light curves in Figs. 1 and 2. In a few cases, the third light derived from the light curve modeling was rather low, close to $\sim 1\%$, while no third body was found from the $O-C$ analysis (as described in detail in Section 5) and vice versa. This is acceptable within error range, especially in the case that we consider possible changes in the $O-C$ diagrams, when adding new data in the future.

4 ABSOLUTE PHYSICAL PARAMETERS

Physical and geometrical parameters were estimated for both binary components using results from the best fits to the observed light curves, as described in the previous section. Physical parameters of contact binaries are highly constrained by their Roche geometry and therefore they follow certain empirical relations (Maceroni et al. 1982; Hilditch et al. 1988; Gazeas & Niarchos 2006; Gazeas & Stepień 2008; Michel & Kjurkchieva 2019). However, in the absence of radial velocity measurements for the majority of the targets, the mass of the primary components in each system had to be estimated empirically. For ultra-short contact binaries it is a serious obstacle for obtaining precise radial velocity measurements, due to the fast rotation of the components, which results in highly broadened and blended spectral lines.

Reasonable estimates for the mass and radius of the primary component can be derived using data for single MS stars, estimated from their temperature or color index (Harmanec 1988; Torres et al. 2010; Pecaut & Mamajek 2013). However, stellar mass is usually underestimated when models of single MS stars are used in calculations. When the binary configuration is imposed in a model, the mass is slightly different. By taking this argument into consideration, we used the empirical relations proposed by Gazeas & Stepień (2008); Gazeas (2009) (Eq. 1 and Eq. 2 respectively), in order to determine the mass of the primary components and calculate an average value from these estimations. In these equations the mass is calculated in solar units, while orbital period in days, respectively.

$$\log M_1 = 0.755(59)\log P + 0.416(24) \quad (1)$$

$$\log M_1 = 0.725(59)\log P - 0.076(32)\log q + 0.365(32) \quad (2)$$

The above empirical relations are based on combined spectroscopic and photometric models, as a result of the W UMa Programme (Kreiner et al. 2003) for contact binaries with orbital period ranging from 0.22 to 0.9 days. There is a paucity of ultra-short period systems under the orbital period cut-off limit in the sample used to derive the empirical relations. However, it is very encouraging that in the cases of two systems for which independent spectroscopic measurements exist, the agreement is very good. More specifically, the systems 1SWASP J093010.78+533859.5 and 1SWASP J150822.80-054236.9, were observed spectroscopically by Lohr et al. (2015a) and Lohr et al. (2014) and the primary mass values retrieved from these studies were $M_1 = 0.86 \pm 0.02$ and $M_1 = 1.07^{+0.12}_{-0.09}$ respectively. As seen in Table 3 our approach concluded in similar masses of $M_1 = 0.852 \pm 0.005$ and $M_1 = 0.931 \pm 0.007$ respectively.

The physical parameters of all systems studied in this work are given in Table 3. In this table, we use the designation "1" for the more massive component, resulting always in a mass ratio less than unity. In cases where the mass ratio was found greater than 1 (see Tables in Appendix A), the mass ratio was inverted in order to produce a uniform sample for all systems. This inversion occurred in 10 out of the 30 systems in this sample. There is no physical difference between systems with $q < 1$ and $q > 1$. This is a result of the photometric definition of the primary minimum, which is always set as the deeper one. Radial velocity measurements can only resolve this issue and clarify which component is the more massive one.

5 ORBITAL PERIOD MODULATION

It is very common for contact binaries to exhibit orbital period modulations. Detailed study of these modulations is a useful tool to investigate the dynamical evolution of binary systems and search for companions. The most frequently observed period modulations are either parabolic, cyclic, or both. The secular period modulations are associated either with mass transfer between the components or mass loss through stellar winds. The cyclic modulation of the orbital period can be attributed to a third body orbiting the system or to magnetic braking in the components' envelope caused by the Applegate mechanism (Applegate 1992).

A thorough study of $O-C$ diagrams is the best way to detect possible period variations and study their orbital parameters. Nonetheless, the accuracy of the parameters that could be derived from $O-C$ diagrams, depends significantly on the time span of observations. Very short time scales (of the order of a few years) could easily lead to wrong conclusions. That is why, a significant effort was made to gather as many times of minimum light as possible (following the procedure mentioned in section 3.1) for each target leading to a more robust conclusion.

In order to construct the $O-C$ diagrams, the linear ephemeris is used (equation 3) with the updated values of orbital period from Table 1. When the linear ephemeris could not describe long-term trends in the $O-C$ diagrams, equations 4 and 5 were used to account for parabolic trends and cyclic variations, respectively. This procedure was carried out by using the *LITE* software (Zasche et al. 2009) that calculates period modulations, while taking into consideration the statistical weight of each time of minimum. The coefficients that appear in equations 4 and 5 are described as follows: b is the quadratic coefficient linked to the orbital period change rate,

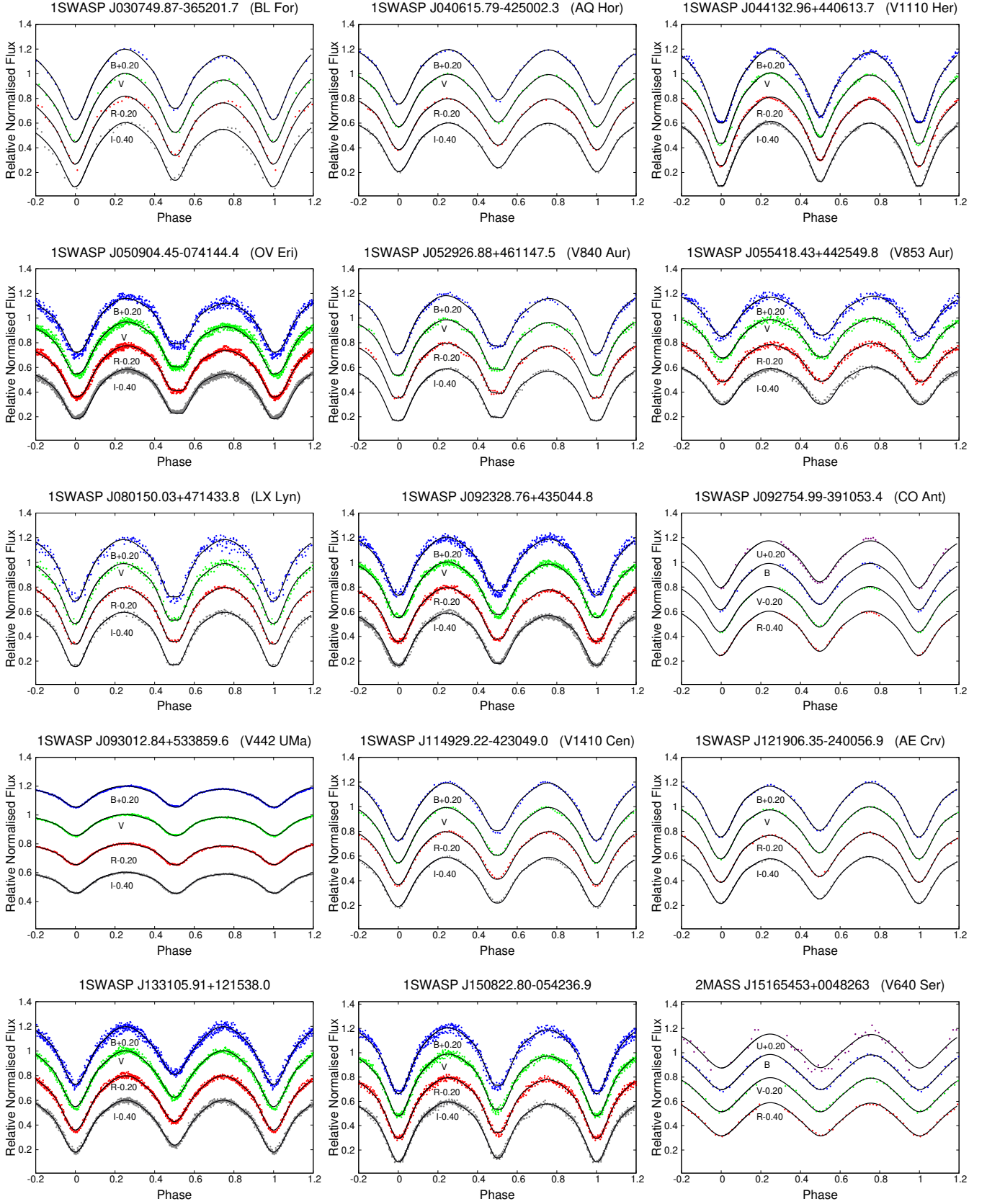


Figure 1. Observed (points) and theoretical (lines) light curves for the 15 systems of our sample in four bands (*BVRI* or *UBVR* filters). The light curves are shifted vertically for clarity.

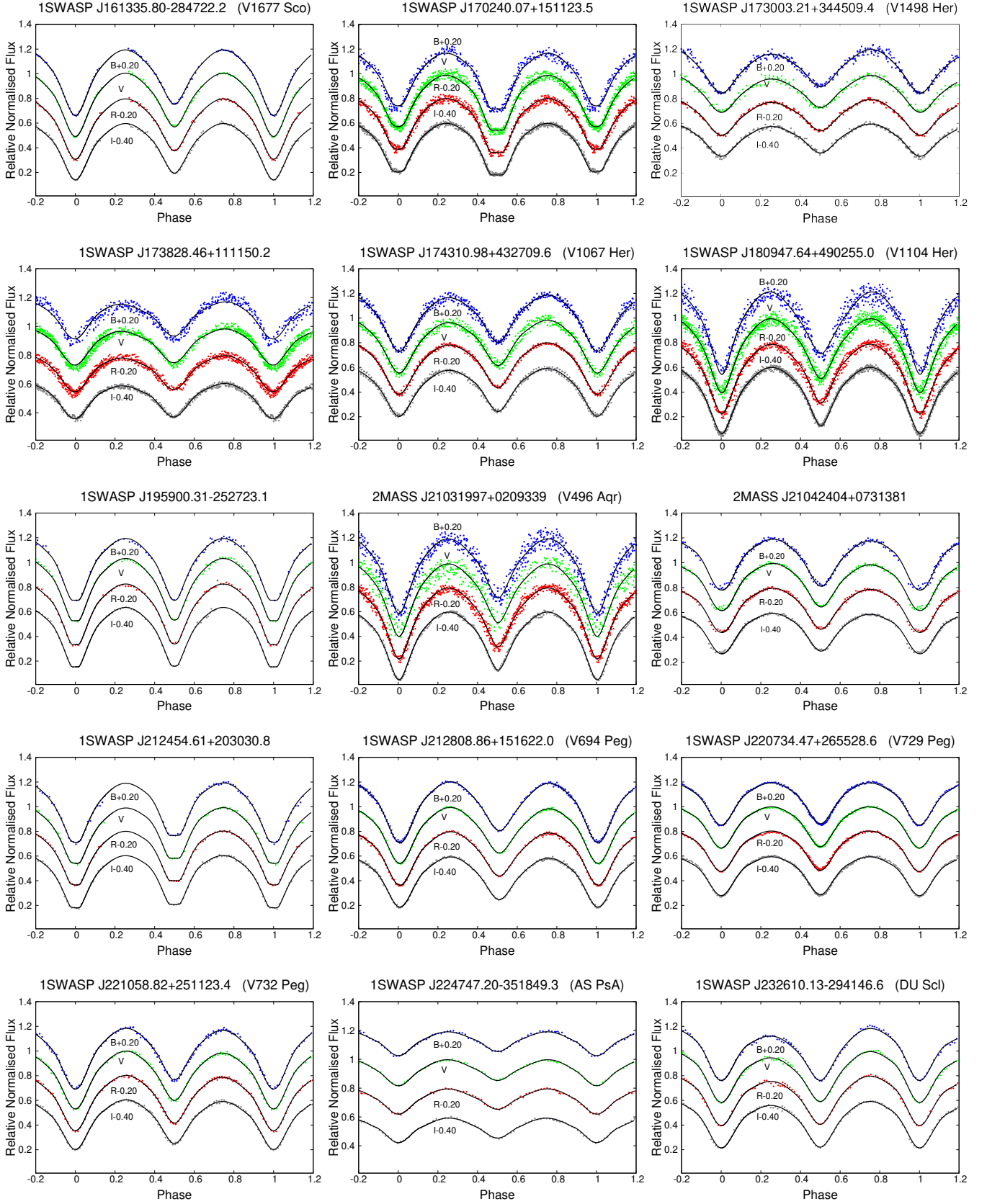


Figure 2. The same as Fig. 1 for the rest 15 systems in our sample.

Table 3. Absolute parameters (in solar units) and their errors of the systems studied in the present paper. Subscripts 1 refers to the larger and more massive component, while subscript 2 refers to the smaller and less massive one.

System ID	$\mathcal{M}_1 (M_\odot)$	$\mathcal{M}_2 (M_\odot)$	$R_1 (R_\odot)$	$R_2 (R_\odot)$	$L_1 (L_\odot)$	$L_2 (L_\odot)$
1SWASP J030749.87-365201.7	0.838 ± 0.007	0.465 ± 0.055	0.782 ± 0.029	0.570 ± 0.021	0.267 ± 0.050	0.128 ± 0.024
1SWASP J040615.79-425002.3	0.821 ± 0.009	0.536 ± 0.034	0.735 ± 0.015	0.576 ± 0.012	0.279 ± 0.047	0.128 ± 0.023
1SWASP J044132.96+440613.7	0.837 ± 0.010	0.545 ± 0.022	0.739 ± 0.009	0.667 ± 0.009	0.401 ± 0.061	0.260 ± 0.042
1SWASP J050904.45-074144.4	0.863 ± 0.003	0.281 ± 0.006	0.813 ± 0.005	0.461 ± 0.004	0.371 ± 0.059	0.118 ± 0.019
1SWASP J052926.88+461147.5	0.850 ± 0.002	0.327 ± 0.003	0.797 ± 0.003	0.490 ± 0.004	0.484 ± 0.072	0.174 ± 0.026
1SWASP J055416.98+442534.0	0.844 ± 0.010	0.193 ± 0.009	0.812 ± 0.007	0.393 ± 0.005	0.449 ± 0.069	0.107 ± 0.016
1SWASP J080150.03+471433.8	0.819 ± 0.003	0.369 ± 0.010	0.751 ± 0.006	0.496 ± 0.005	0.237 ± 0.041	0.109 ± 0.019
1SWASP J092328.76+435044.8	0.870 ± 0.003	0.356 ± 0.005	0.824 ± 0.004	0.523 ± 0.004	0.688 ± 0.095	0.275 ± 0.038
1SWASP J092754.99-391053.4	0.837 ± 0.005	0.428 ± 0.003	0.769 ± 0.002	0.539 ± 0.003	0.450 ± 0.067	0.186 ± 0.029
1SWASP J093010.78+533859.5	0.852 ± 0.005	0.338 ± 0.006	0.803 ± 0.054	0.502 ± 0.034	0.282 ± 0.061	0.12 ± 0.026
1SWASP J114929.22-423049.0	0.855 ± 0.002	0.293 ± 0.042	0.810 ± 0.029	0.473 ± 0.017	0.174 ± 0.036	0.055 ± 0.012
1SWASP J121906.35-240056.9	0.847 ± 0.001	0.344 ± 0.024	0.787 ± 0.044	0.538 ± 0.030	0.260 ± 0.053	0.092 ± 0.020
1SWASP J133105.91+121538.0	0.816 ± 0.005	0.424 ± 0.043	0.754 ± 0.023	0.533 ± 0.016	0.358 ± 0.060	0.140 ± 0.025
1SWASP J150822.80-054236.9	0.931 ± 0.007	0.475 ± 0.030	0.874 ± 0.052	0.611 ± 0.036	0.481 ± 0.094	0.232 ± 0.045
2MASS J15165453+0048263	0.814 ± 0.005	0.237 ± 0.016	0.742 ± 0.021	0.555 ± 0.016	0.706 ± 0.100	0.381 ± 0.055
1SWASP J161335.80-284722.2	0.840 ± 0.011	0.572 ± 0.070	0.766 ± 0.031	0.612 ± 0.025	0.225 ± 0.044	0.120 ± 0.024
1SWASP J170240.07+151123.5	0.948 ± 0.001	0.328 ± 0.002	0.915 ± 0.003	0.536 ± 0.004	0.468 ± 0.075	0.204 ± 0.031
1SWASP J173003.21+344509.4	0.825 ± 0.010	0.543 ± 0.028	0.749 ± 0.013	0.590 ± 0.010	0.245 ± 0.043	0.125 ± 0.023
1SWASP J173828.46+111150.2	0.922 ± 0.005	0.264 ± 0.001	0.879 ± 0.004	0.463 ± 0.005	0.526 ± 0.080	0.126 ± 0.020
1SWASP J174310.98+432709.6	0.921 ± 0.010	0.538 ± 0.034	0.859 ± 0.017	0.640 ± 0.013	0.522 ± 0.081	0.229 ± 0.038
1SWASP J180947.64+490255.0	0.824 ± 0.017	0.797 ± 0.019	0.764 ± 0.005	0.701 ± 0.005	0.141 ± 0.028	0.095 ± 0.020
1SWASP J195900.31-252723.1	0.870 ± 0.007	0.474 ± 0.023	0.811 ± 0.011	0.586 ± 0.008	0.501 ± 0.074	0.232 ± 0.037
2MASS J21031997+0209339	0.825 ± 0.017	0.819 ± 0.019	0.743 ± 0.004	0.706 ± 0.004	0.186 ± 0.034	0.136 ± 0.026
2MASS J21042404+0731381	0.807 ± 0.005	0.247 ± 0.033	0.751 ± 0.023	0.412 ± 0.013	0.269 ± 0.048	0.079 ± 0.014
1SWASP J212454.61+203030.8	0.849 ± 0.002	0.364 ± 0.006	0.782 ± 0.004	0.503 ± 0.004	0.416 ± 0.064	0.174 ± 0.027
1SWASP J212808.86+151622.0	0.838 ± 0.004	0.398 ± 0.040	0.779 ± 0.023	0.527 ± 0.016	0.265 ± 0.048	0.089 ± 0.017
1SWASP J220734.47+265528.6	0.845 ± 0.010	0.560 ± 0.016	0.745 ± 0.005	0.588 ± 0.004	0.287 ± 0.047	0.173 ± 0.029
1SWASP J221058.82+251123.4	0.809 ± 0.002	0.356 ± 0.037	0.750 ± 0.022	0.491 ± 0.015	0.302 ± 0.052	0.102 ± 0.019
1SWASP J224747.20-351849.3	0.806 ± 0.012	0.607 ± 0.014	0.680 ± 0.006	0.548 ± 0.006	0.141 ± 0.026	0.061 ± 0.013
1SWASP J232610.13-294146.6	0.864 ± 0.002	0.291 ± 0.033	0.813 ± 0.022	0.469 ± 0.013	0.327 ± 0.057	0.080 ± 0.015

a_{12} is the projected semi-major axis, i_3 the orbital inclination of the tertiary component with respect to the system's orbital plane, c the speed of light, e_3 the eccentricity of the orbit of the tertiary component around the centre of mass, ω_3 the longitude of periastron and ν is the true anomaly around the centre of mass of the triple system.

$$(O - C)_1 = T - (T_0 + P \times E) \quad (3)$$

$$(O - C)_2 = (O - C)_1 - b \times E^2 \quad (4)$$

$$(O - C)_3 = (O - C)_2 - \frac{a_{12} \sin i_3}{c} \left[\frac{1 - e_3^2}{1 + e_3 \cos \nu} \sin(\nu + \omega_3) + e_3 \sin \omega_3 \right] \quad (5)$$

In this study it is found that five systems out of 30 (i.e. 17 per cent) exhibit no change in their orbital period, as they show no modulation in their $O - C$ diagrams (Fig. 3).

Orbital period modulations are shown in 12 out of 30 systems (40 per cent of the sample) out of which 6 present negative orbital period rates for downward parabola shape in the $O - C$ diagram and 6 positive period rates for upward parabola shape respectively. This finding, gives no conclusive evidence that the ultra-short orbital period systems tend to shrink their orbits, through the decrease of their orbital period. Eight of the above systems (27 per cent of the entire sample) present only secular orbital systematic period modulation (with negative or positive dP/dt) with no additional component, as shown in Figs. 4 and 5.

Furthermore, from the $O - C$ analysis it was found that 13 systems (43 per cent) host a third component in a wider orbit around

them, with no change in orbital period, while four systems (13 per cent) host a third component with change in orbital period (Figs. 6 with 7 and 8, respectively). The existence of the third component is also supported by the third light, found in the light curve models. The fact that the above 17 systems (57 per cent) host a third component, comes in agreement with D'Angelo et al. (2006) who found that more than 30 per cent of contact binary systems belong to triple systems and have a spectroscopic signature of a third component. It seems that more systems can be characterised as triples by means of the $O - C$ analysis, as it is more sensitive in detecting eclipse time variations. The results of the $O - C$ analysis, i.e. the period of the tertiary component (P_3), the amplitude of the cyclic variation (A), the value of $a_{12} \sin i_3$ and the possible minimum mass of the tertiary component in a co-planar orbit (M_{3min}), are presented in Table 4.

For 12 systems that exhibit secular period changes, we have computed the mass transfer and mass loss rates, using the software provided by Liakos (2015). Secular orbital period increase (positive dP/dt) can be caused either by mass transfer from the less massive component to the more massive one or by mass loss from the system through stellar winds. On the contrary, orbital period decrease (negative dP/dt) is typically caused by mass transfer of the more massive component to the less massive one. For systems that present period increase in their $O - C$ diagrams, and given that we cannot be certain which is the driving mechanism, both mass transfer (dM_T/dt) and mass loss (dM_L/dt) mechanisms can be applied (Table 4). It should be mentioned that these two mechanisms are not taking place in a binary at the same time. Typically, the values

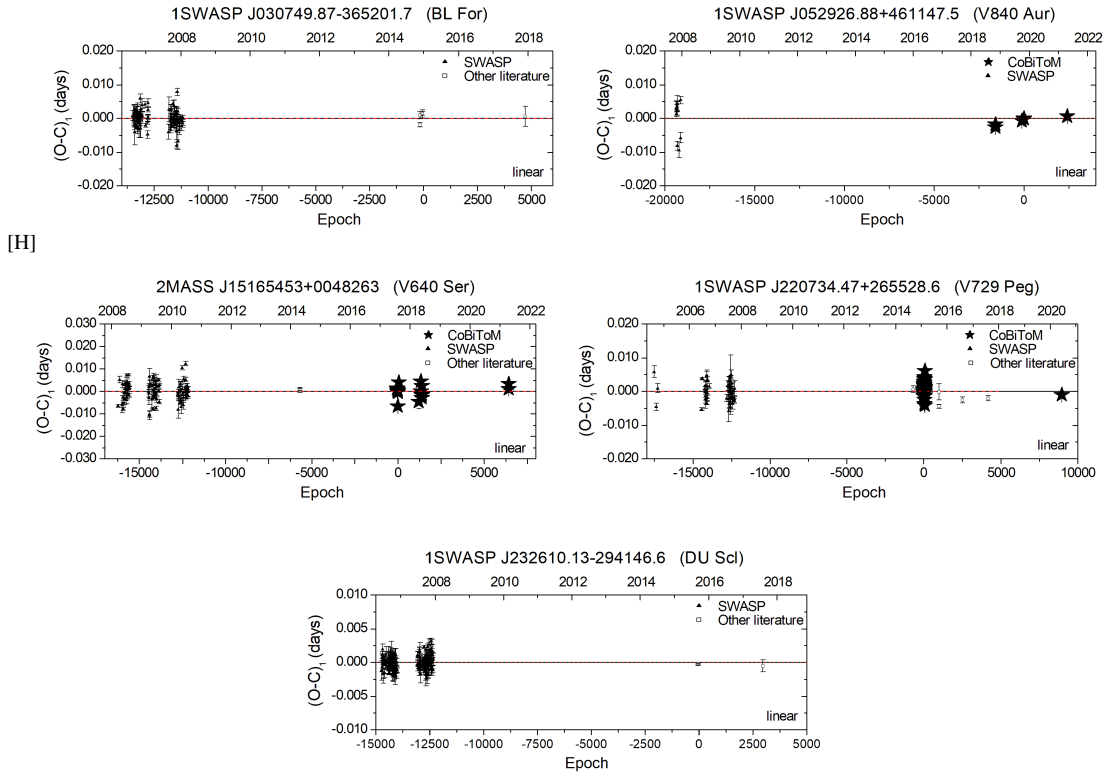


Figure 3. The $O - C$ diagrams for the five systems of the sample that present circular orbits with no additional effects.

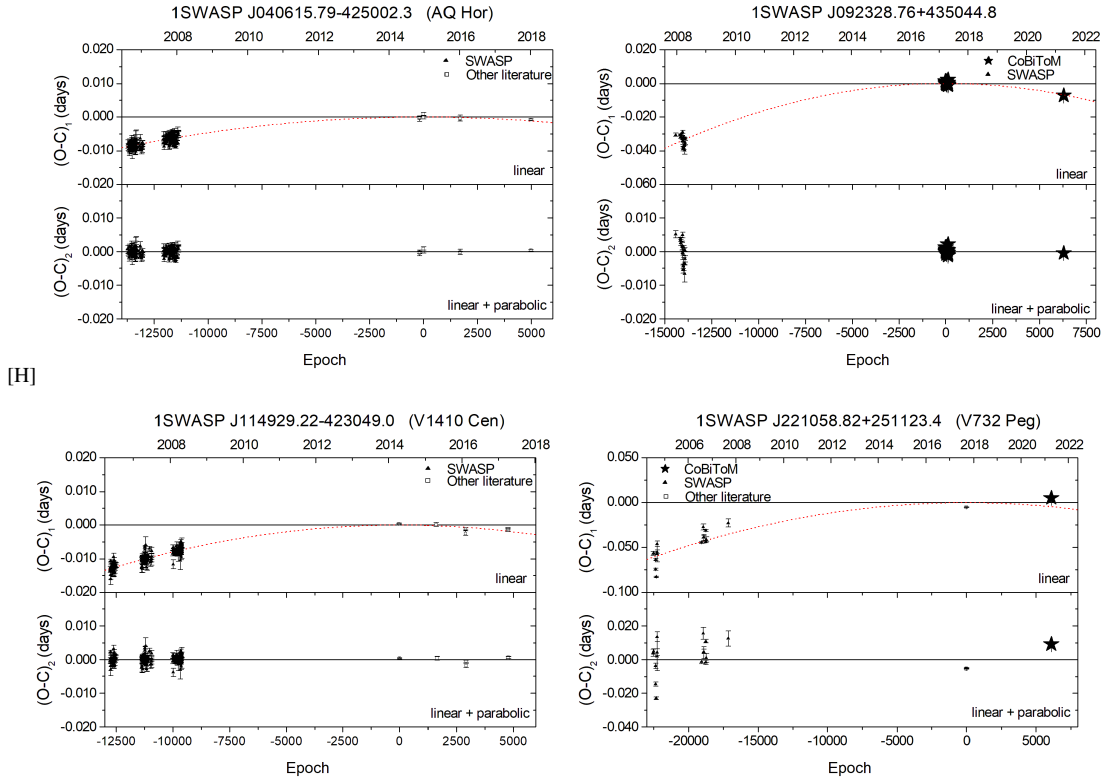


Figure 4. The $O - C$ diagrams for the four systems that present circular orbits with prominent negative second order period modulation.

Table 4. Orbital period modulation parameters, as derived from the $O - C$ diagram analysis, accompanied with the corresponding mass transfer and mass loss rates.

System ID	P_3 (yr)	A (days)	$M_{3 \text{ min}}$ (M_\odot)	$a_{12} \sin i_3$ (AU)	\dot{P} ($10^{-7} \text{ d yr}^{-1}$)	dM_T/dt ($10^{-7} M_\odot \text{ yr}^{-1}$)	dM_L/dt ($10^{-7} M_\odot \text{ yr}^{-1}$)
1SWASP J030749.87-365201.7	–	–	–	–	–	–	–
1SWASP J040615.79-425002.3	–	–	–	–	-1.526 ± 0.221	-2.85 ± 0.73	–
1SWASP J044132.96+440613.7	15.86 ± 5.05	0.0104 ± 0.0042	0.53 ± 0.14	2.039 ± 0.817	–	–	–
1SWASP J050904.45-074144.4	–	–	–	–	0.350 ± 0.241	0.21 ± 0.15	-0.86 ± 0.59
1SWASP J052926.88+461147.5	–	–	–	–	–	–	–
1SWASP J055416.98+442534.0	8.59 ± 0.24	0.0023 ± 0.0001	0.18 ± 0.01	0.669 ± 0.039	–	–	–
1SWASP J080150.03+471433.8	9.76 ± 1.52	0.0109 ± 0.0031	0.66 ± 0.01	1.989 ± 0.561	0.797 ± 0.067	0.82 ± 0.08	-2.17 ± 0.18
1SWASP J092328.76+435044.8	–	–	–	–	-5.329 ± 0.579	-4.51 ± 0.29	–
1SWASP J092754.99-391053.4	17.62 ± 1.12	0.0042 ± 0.0007	0.13 ± 0.01	0.736 ± 0.125	–	–	–
1SWASP J093010.78+533859.5	14.50 ± 0.01	0.0023 ± 0.0001	0.08 ± 0.01	0.402 ± 0.015	–	–	–
1SWASP J114929.22-423049.0	–	–	–	–	-2.562 ± 0.217	-1.66 ± 0.39	–
1SWASP J121906.35-240056.9	14.90 ± 1.74	0.0029 ± 0.0018	0.11 ± 0.02	0.596 ± 0.372	–	–	–
1SWASP J133105.91+121538.0	150.18 ± 84.99	0.0018 ± 0.0001	0.15 ± 0.02	3.049 ± 0.018	–	–	–
1SWASP J150822.80-054236.9	3.86 ± 0.04	0.0010 ± 0.0001	0.10 ± 0.01	0.182 ± 0.007	–	–	–
2MASS J15165453+0048263	–	–	–	–	–	–	–
1SWASP J161335.80-284722.2	8.89 ± 0.45	0.0025 ± 0.0009	0.15 ± 0.06	0.461 ± 0.176	-5.525 ± 0.035	-44.6 ± 32.4	–
1SWASP J170240.07+151123.5	–	–	–	–	2.408 ± 0.444	1.52 ± 0.28	-5.78 ± 1.07
1SWASP J173003.21+344509.4	9.55 ± 0.01	0.0043 ± 0.0002	0.27 ± 0.01	0.866 ± 0.031	-5.848 ± 0.001	-13.9 ± 2.12	–
1SWASP J173828.46+111150.2	–	–	–	–	12.25 ± 1.74	5.97 ± 0.86	-28.7 ± 4.07
1SWASP J174310.98+432709.6	49.02 ± 3.20	0.0092 ± 0.0002	0.22 ± 0.01	2.099 ± 0.038	–	–	–
1SWASP J180947.64+490255.0	8.35 ± 0.19	0.0012 ± 0.0001	0.11 ± 0.01	0.324 ± 0.016	–	–	–
1SWASP J195900.31-252723.1	28.73 ± 15.18	0.0081 ± 0.0022	0.29 ± 0.05	1.568 ± 0.416	–	–	–
2MASS J21031997+0209339	10.64 ± 0.51	0.0045 ± 0.0006	0.25 ± 0.01	0.793 ± 0.102	–	–	–
2MASS J21042404+0731381	2.78 ± 0.05	0.0027 ± 0.0001	0.28 ± 0.01	0.460 ± 0.001	3.291 ± 0.001	1.86 ± 0.36	-8.27 ± 0.09
1SWASP J212454.61+203030.8	8.78 ± 0.94	0.0038 ± 0.0020	0.28 ± 0.01	0.683 ± 0.367	–	–	–
1SWASP J212808.86+151622.0	13.57 ± 1.52	0.0017 ± 0.0004	0.06 ± 0.01	0.286 ± 0.075	–	–	–
1SWASP J220734.47+265528.6	–	–	–	–	–	–	–
1SWASP J221058.82+251123.4	–	–	–	–	-4.098 ± 1.875	-21 ± 9.8	–
1SWASP J224747.20-351849.3	–	–	–	–	5.445 ± 0.729	20.7 ± 3.51	-17.7 ± 2.38
1SWASP J232610.13-294146.6	–	–	–	–	–	–	–

of mass transfer/loss rate found in contact binaries are of the order $10^{-7} M_\odot \text{ yr}^{-1}$ (Kouzuma 2018; Li et al. 2020).

According to previous studies (Kubiak et al. 2006; Lohr et al. 2015b; Pietrukowicz et al. 2017) contact binaries could exhibit both period decrease and period increase. Lohr et al. (2015b) presented a statistical analysis on contact binaries from SWASP data, where the \dot{P} is almost evenly distributed in both positive and negative values. Similar distribution of \dot{P} is observed in the present study. However in the present study no extreme values of \dot{P} were found compared to the study of Lohr et al. (2015b), which is probably due to the different time range.

$O - C$ diagrams could also be a very useful tool to determine whether the contact binary is a member of a triple or even a multiple system. Literature studies suggest that the number of the detected tertiary components in contact binary systems is increasing (e.g. Pribulla & Rucinski 2006; D’Angelo et al. 2006; Tokovinin et al. 2006; Rucinski et al. 2007). In our investigation, more than half of the sample (17 systems) have shown cyclic period variations, complying with the light curve model findings of third light. Interestingly, none of them satisfy the criterion of Lanza & Rodonò (2002) regarding the quadrupole moment variation value of the components that is needed for the Applegate mechanism (Applegate 1992) to explain the observed cyclic orbital period changes. Therefore, the cyclic variations in our sample can be interpreted exclusively by the presence of tertiary components.

In a few cases, the minimum mass of the possible third component is less than $0.1 M_\odot$, which could indicate the presence of a brown dwarf or even a hot Jupiter. Therefore, long-term monitoring

of these ultra-short contact binaries is essential, not only to detect any intrinsic period changes, but also to specify whether or not they belong to triple or even multiple stellar systems.

6 DISCUSSION

In the present study we have provided results from 4-band photometry for 30 ultra-short orbital period contact binaries, which are very close to the period cut-off (less than 0.26 d). A strong asset of observing campaigns such as the *CoBiToM Project*, is the long term monitoring of several contact binaries and the thorough investigation derived from the light curve and orbital period modulation analysis. Future spectroscopy for the determination of the radial velocities of both components is certainly desirable and will help to verify our results. In the following subsections, the topics that have been investigated in our study are summarised.

6.1 Darwin Instability

Darwin instability is one of the physical mechanisms proposed to lead a binary to a merger (e.g. the case of the red nova progenitor V1309 Sco merger Tyndra et al. 2011, 2013). This instability appears when the binary exhibits orbital angular momentum loss and the total angular momenta exceed the value of one third of the spin of the primary component. Then, synchronous rotation ceases to exist. The binary enters a very unstable phase and the coalescence between the components is highly probable. Therefore, a check was made on the dynamical instability in each system of our sample.

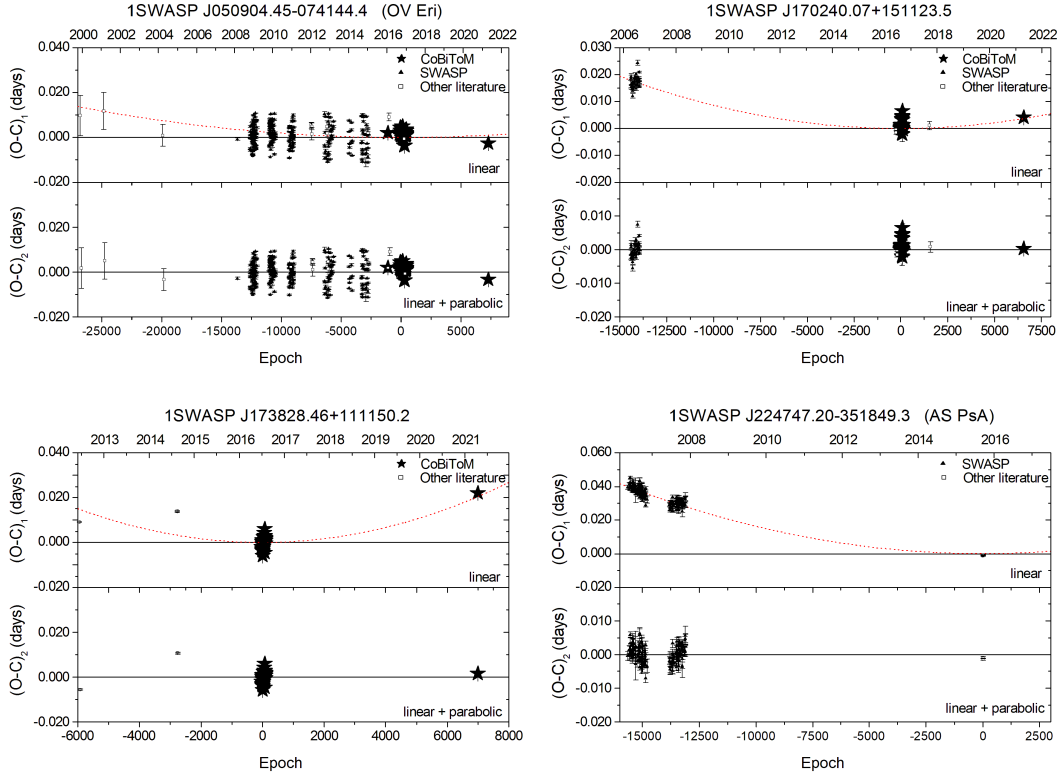


Figure 5. The $O - C$ diagrams for the four systems that present circular orbits with prominent positive second order period modulation.

The spin angular momentum can be calculated for both components, while the orbital one can be derived for the entire system, by using the Eq. 6 and Eq. 7, respectively. In order to examine if this instability favors targets in our sample, we calculated the orbital and spin angular momenta. First, we consider that the systems in our sample are in synchronous rotation (as expected for contact binary systems) and we assume that the gyration radii are the same for the two components and equal to $k^2 = 0.06$ according to Rasio (1995). Then, the ratio of the spin angular momentum to the orbital angular momentum was computed using the Eq. 8.

$$J_{spin} = (k_1^2 M_1 R_1^2 + k_2^2 M_2 R_2^2) \omega_s, \quad (6)$$

$$J_{orb} = \frac{M_1 M_2}{M_1 + M_2} a^2 \omega_o \quad (7)$$

$$\frac{J_{spin}}{J_{orb}} = k^2 \left(\frac{1+q}{q} \right) \left(\frac{R_1}{a} \right)^2 \left(1 + q \left(\frac{R_2}{R_1} \right)^2 \right) \quad (8)$$

Approximations on the effective radius of each Roche lobe (r_L) were used, using Eq. 9 for filling the inner Roche lobe and Eq. 10 for filling the outer Roche lobe, according to the expressions mentioned in Eggleton (1983) and Yakut & Eggleton (2005). These boundaries were used to calculate respective limits of the spin angular momentum to the orbital angular momentum ratio, when the contact binary has filled the inner or the outer Roche lobes.

$$r_{L \text{ inner}} = \frac{0.49q^{2/3}}{0.6q^{2/3} + \ln(1 + q^{1/3})} \quad (9)$$

$$r_{L \text{ outer}} = \frac{0.49q^{2/3} + 0.27q - 0.12q^{4/3}}{0.6q^{2/3} + \ln(1 + q^{1/3})} \quad (10)$$

In Fig. 9 these theoretical boundaries are depicted for the uniform sample of contact binary systems from Gazeas et al. (2021a) and our sample. A similar investigation was made by Li & Zhang (2006), but without accounting for ultra-short contact binaries. Darwin instability favours only systems with extreme mass ratio values close to 0.07 (Li & Zhang 2006) and ultra-short contact binaries do not present extreme values. Fig. 9 can be an observational confirmation of the theoretical prediction of Stępień (2006); Stępień & Gazeas (2012), that the ultra-short binary systems are evolving with a very slow pace, without having enough time to reach the final coalescence, as this process takes several Gyrs. A long evolutionary time is needed for ultra-short contact binaries to reach such an extremely small mass ratio and become dynamically unstable. Nevertheless, Darwin instability should take place during the very final stages of the possible merger process, as the binary could not maintain such an unstable orbit and asynchronous rotation.

6.2 Orbital Period Modulations

It is found that 40 per cent of the systems in the present study are accompanied by some amount of third light (either due to a close visual companion, or being members of triple or multiple systems). This result is also confirmed by the $O - C$ analysis, where 57 per cent of the entire sample is found to host a third component, causing the eclipse timings to vary through epochs (as seen through the LITE effect). The $O - C$ study shows that ultra-short period systems seem to have very stable orbits and they do not show evidence

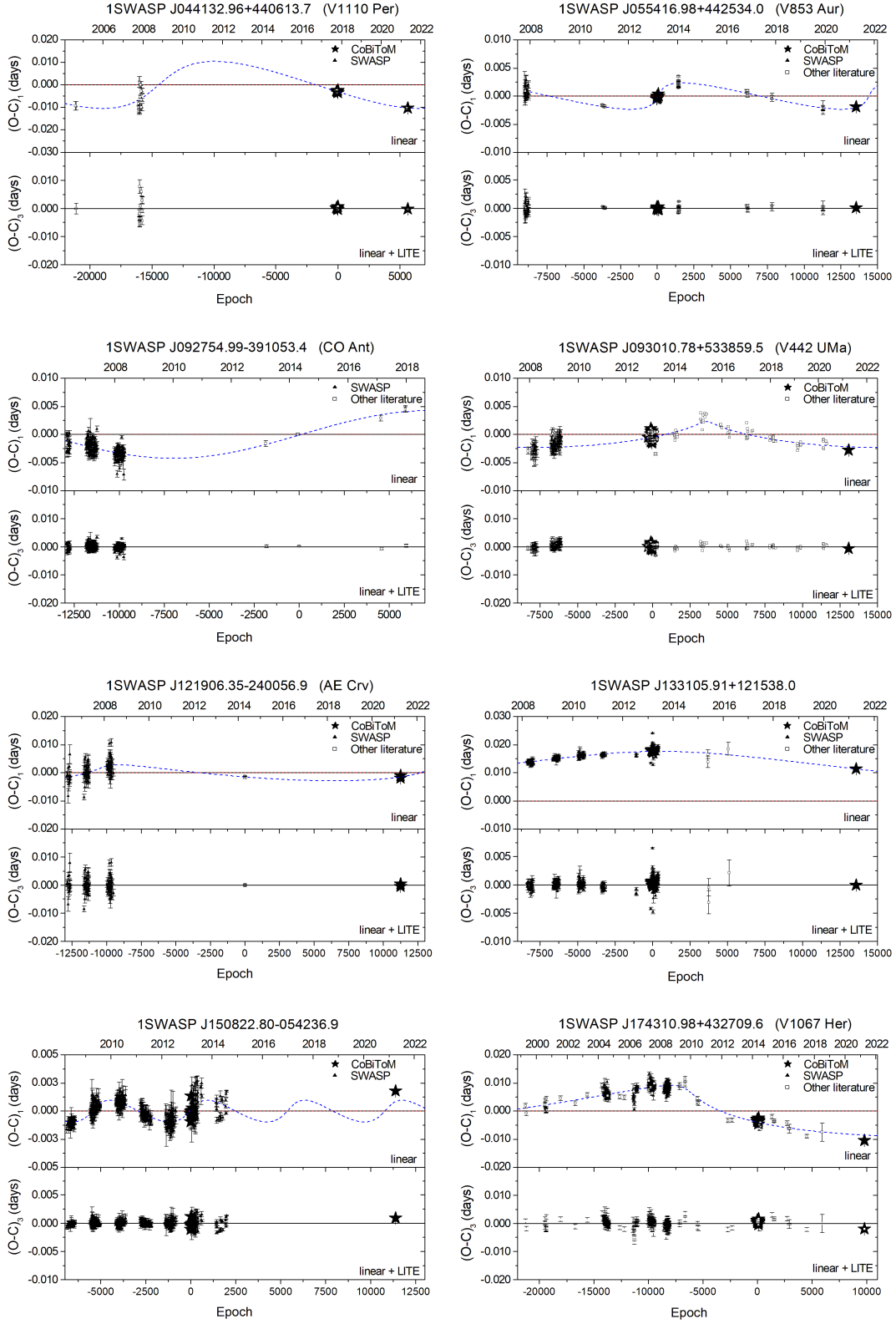


Figure 6. The $O - C$ diagrams for the eight systems of the sample that present circular orbits with presence of an additional cyclic period modulation.

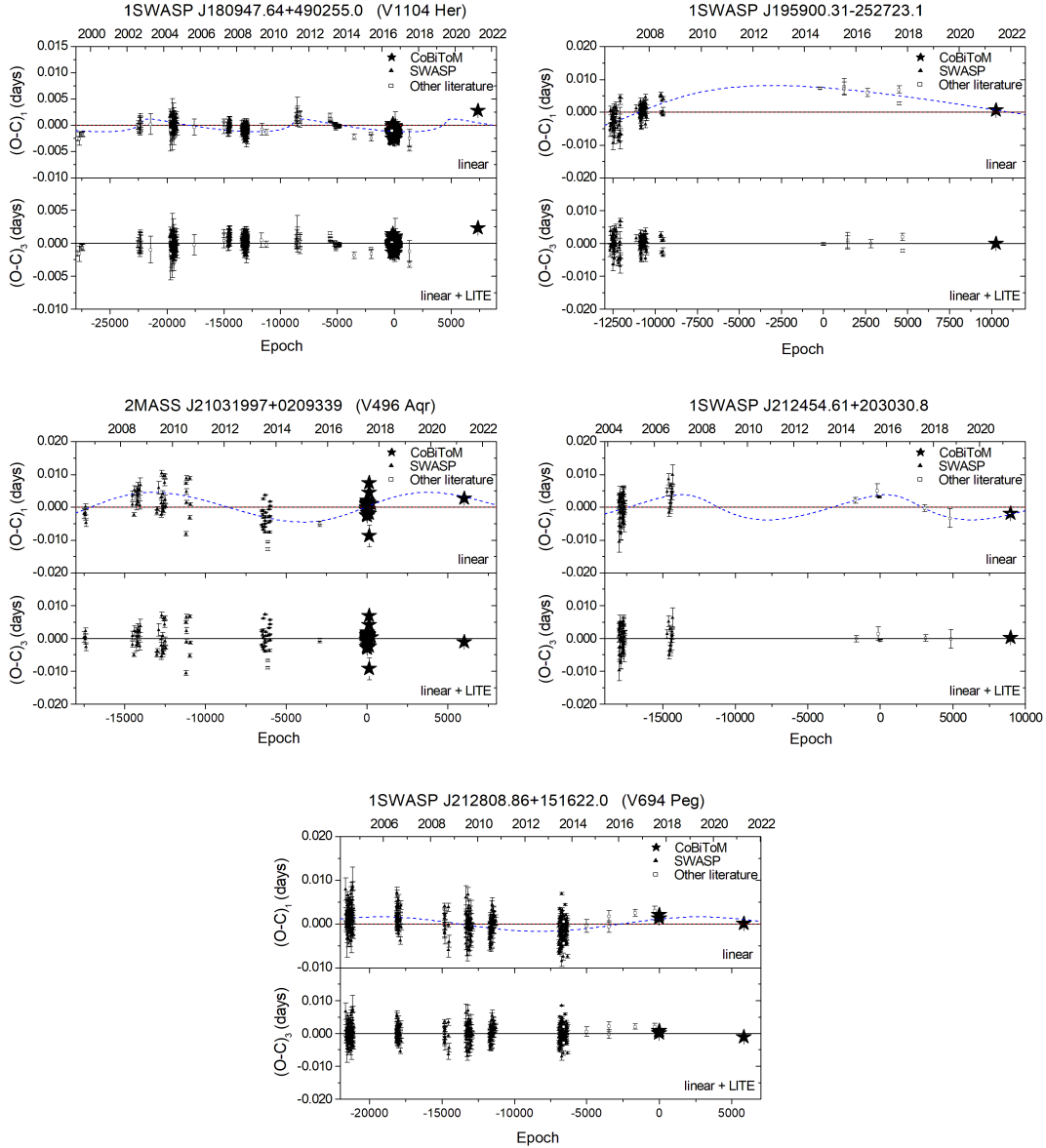


Figure 7. The same as Fig. 6 for the rest five systems that present circular orbits with presence of an additional cyclic period modulation.

of coalescence. The existence of both negative and positive period modulation provides no conclusive evidence that the ultra-short orbital period systems shrink their orbits. The additional component does not seem to affect the orbit, at least in short time scales, which indicates a very slow process and orbital modulation.

The negative parabolic coefficient (i.e. downward parabolic trend in $O - C$ diagrams) is an indication of a shrinking orbit, but not a conclusive evidence. A parabolic trend could also be a part of a longer periodic modulation, while the $O - C$ data of the studied systems cover a period of 17-20 yrs in the best case. This effect could also imply that an even larger fraction of systems containing tertiary components can exist, compared to the fraction that was found in the current or older studies.

This information can only be retrieved, when more data are collected in the forthcoming decades and the time span is increased significantly. Therefore, the results listed in Table 4 are based only on the currently available data.

6.3 Magnetic Activity

The systems in the current sample host cool stellar components of G and K spectral type, which frequently present spotted surfaces due to their magnetic activity. This is confirmed by the asymmetries and the temporal variability of the light curves in 19 out of 30 systems (63 per cent). As already mentioned, the Applegate mechanism does not seem to be applicable on the very low mass stars and it cannot explain the periodic modulation of $O - C$ diagrams. Even though most of the contact binaries of our sample include spots on their common envelopes, the Applegate mechanism is inadequate for explaining the orbital period modulation. Hence, the periodic behavior of $O - C$ diagrams are most likely a result of the LITE effect, caused by the existence of additional components orbiting around the systems.

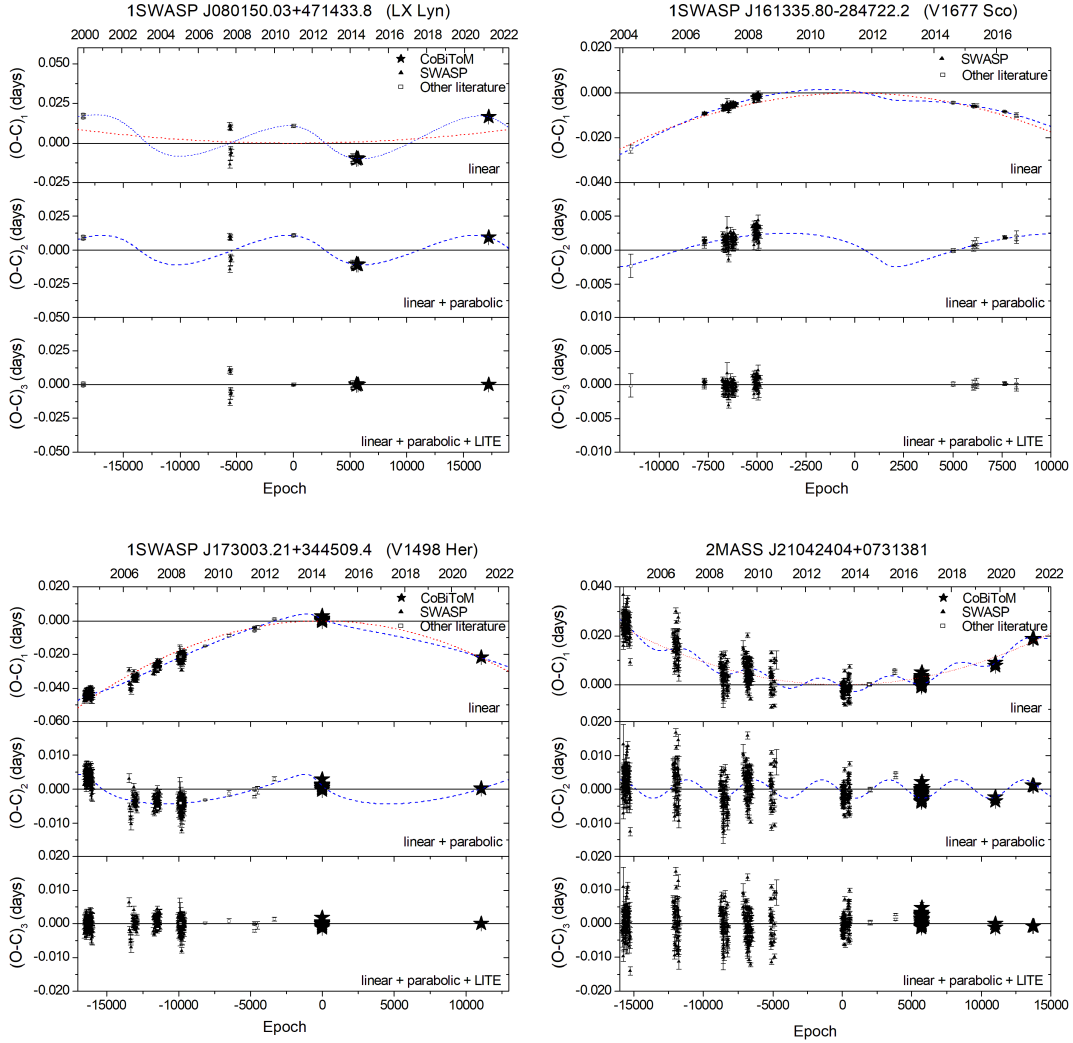


Figure 8. The $O - C$ diagrams for the four systems of the sample that present circular orbits with presence of a second order and a cyclic period modulation.

6.4 Absolute Physical and Orbital Parameters

Ultra-short orbital period contact binaries are among the systems with the smallest and faintest (in terms of size, mass and luminosity) low temperature components. [Stępień & Gazeas \(2012\)](#) showed that these systems host evolved secondaries, which are most probably the product of a mass reversal episode some Gyrs ago.

In this study we found that ultra-short orbital period contact binaries do not reach extremely low mass ratio values and all of them range between the values 0.2 and 1.0 (Fig. 10). The primary mass ranges between 0.80 and 0.93 M_{\odot} and the secondary mass ranges between 0.19 and 0.82 M_{\odot} . The primary's and secondary's radius is also less than 1 R_{\odot} , making the ultra-short orbital period contact binaries those with the smallest values of absolute physical parameters, amongst the entire sample of contact binaries known to date. Our study also showed that the total mass in half of the systems in this sample is below the instability mass limit, as set by [Jiang et al. \(2012\)](#). Moreover, six of these systems also have an orbital period shorter than 0.22 d. Although these systems were considered to have unstable orbits and are heading towards merg-

ing, we found that they are very stable, and in a quite early contact phase.

[Gazeas et al. \(2021a\)](#) showed an interesting trend in the fill-out factor parameter, as compared with the orbital period and mass ratio. It appears that systems with shorter orbital periods tend to have shallow contact configurations. The few well-studied systems (up to that date) with orbital period less than 0.3 d are indeed in shallow contact with fill-out factors less than 25 per cent. The present study confirmed the above finding for all 30 systems. Fig. 10 shows the correlation between the orbital and physical parameters, i.e. the mass ratio as a function of the orbital period, the fill-out factor as a function of the mass ratio and the mass ratio as a function of the orbital period. The f and q parameters are derived from the light curve modeling (Tables in Appendix A). According to our results, none of the studied systems appears to be in deep contact configuration. Two systems (1SWASP J220734.47+265528.6 & 1SWASP J224747.20-351849.3) appear to be in marginal contact, indicating that they have probably just entered the contact phase of their evolution. The low fill-out factor in these systems could plausibly be explained by assuming that the systems are evo-

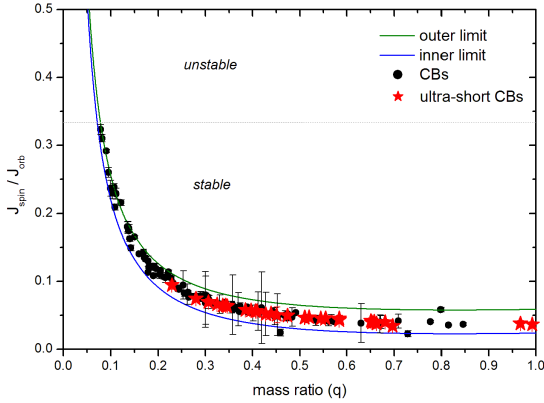


Figure 9. The spin to orbital angular momentum ratio is plotted against the mass ratio q . The solid lines indicate the inner and outer theoretical limits for the systems filling the inner and outer Roche lobe, respectively. The filled black points represent the sample of 138 *W UMa*-type binaries from Gazeas et al. (2021a), while the red star markers represent the ultra-short period binary systems of the present study. The uncertainty on the red star markers is smaller than the marker size.

lutionary young, as suggested by Stepień & Gazeas (2012) and Li et al. (2019).

7 SUMMARY AND CONCLUSIONS

Summarising, contact binary systems with extremely short orbital periods are rare and only a handful of such systems are known and well studied up to date. Their components follow the MS trend and they are located within the ZAMS and TAMS limits. The absence of deep contact configuration, the fact that there is no particular preference in orbital period modulation and the presence of very stable orbits in terms of angular momentum and Darwin criteria, lead to the conclusion that ultra-short period systems show no evidence of merging. Low mass-ratio systems seem more promising candidates for giving such an evidence, which could possibly lead towards the detection of red nova progenitors among them. Long-term monitoring of orbital parameters through $O - C$ diagrams could reveal the existence of a possible orbital substantial secular change, which could eventually lead to their merger into single fast-rotating stars.

ACKNOWLEDGEMENTS

This research is co-financed by Greece and the European Union (European Social Fund-ESF) through the Operational Programme ‘Human Resources Development, Education and Lifelong Learning’ in the context of the project ‘Strengthening Human Resources Research Potential via Doctorate Research’ (MIS-5000432), implemented by the State Scholarships Foundation (IKY). This work utilizes data from the robotic and remotely controlled telescope of the University of Athens Observatory (UOAO), located at the National and Kapodistrian University of Athens, Greece. Part of this work is also based on observations obtained with the 1.2 m Kryoneri telescope, located at Corinthia, Greece and the 2.3 m Aristarchos telescope, located at Helmos Observatory, Achaia, Greece. Both telescopes are operated by the Institute for

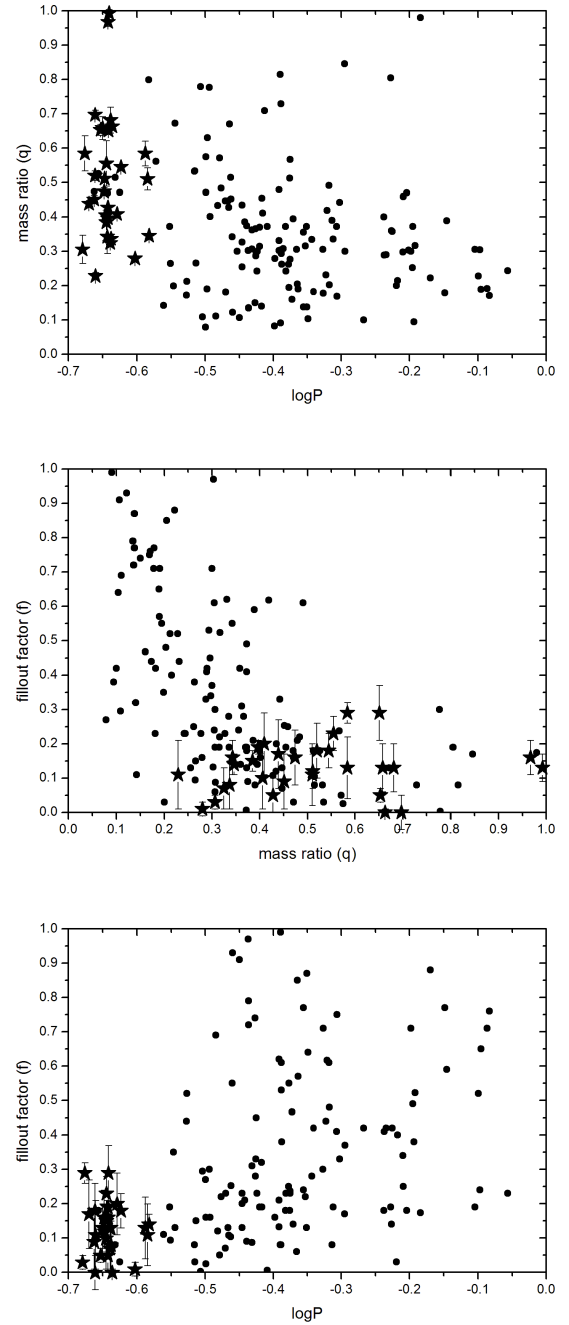


Figure 10. The upper panel shows the distribution of mass ratio as a function of the orbital period, the middle panel shows the distribution of fill-out factor across the mass ratio and the lower panel shows the distribution of fill-out factor across the orbital period. In all panels filled points represent the entire sample of 138 contact binaries, as derived from *W UMa Programme*, while star markers represent the 30 systems of our sample.

Astronomy, Astrophysics, Space Applications and Remote Sensing of the National Observatory of Athens. The authors wish to thank Prof. A. Norton who reviewed the current manuscript and gave valuable comments that improved our work, as well as the collaborators at the observing facilities for their support and the telescope time allocation.

DATA AVAILABILITY

The data underlying this article are available upon request to the corresponding author.

REFERENCES

- Applegate J. H., 1992, *ApJ*, **385**, 621
- Aumer M., Binney J. J., 2009, *MNRAS*, **397**, 1286
- Casagrande L., et al., 2020, arXiv e-prints, p. [arXiv:2011.02517](https://arxiv.org/abs/2011.02517)
- Chen X., Wang S., Deng L., de Grijs R., Yang M., Tian H., 2020, *ApJS*, **249**, 18
- Claret A., Bloemen S., 2011, *A&A*, **529**, A75
- Covey K. R., et al., 2007, *AJ*, **134**, 2398
- D'Angelo C., van Kerkwijk M. H., Rucinski S. M., 2006, *AJ*, **132**, 650
- Darwish M. S., Elkhateeb M. M., Nouh M. I., Saad S. M., Hamdy M. A., Beheary M. M., Gadallah K., Zaid I., 2017, *New Astron.*, **50**, 37
- Davenport J. R. A., et al., 2013, *ApJ*, **764**, 62
- Deleuil M., et al., 2018, *A&A*, **619**, A97
- Dimitrov D. P., Kjurkchieva D. P., 2015, *MNRAS*, **448**, 2890
- Djurašević G., Essam A., Latković O., Cséki A., El-Sadek M. A., Abo-Elala M. S., Hayman Z. M., 2016, *AJ*, **152**, 57
- Drake A. J., et al., 2014a, VizieR Online Data Catalog, p. [JApJS/213/9](https://vizier.cfa.harvard.edu/vizier/doc/JApJS/213/9)
- Drake A. J., et al., 2014b, *ApJ*, **790**, 157
- Eggleton P. P., 1983, *ApJ*, **268**, 368
- Elkhateeb M. M., Saad S. M., Nouh M. I., Shokry A., 2014, *New Astron.*, **28**, 85
- Fang X.-H., Qian S., Zejda M., Boonruksar S., Zhou X., Zhu L., Liao W. P., 2019, *PASJ*, **71**
- Gaia Collaboration et al., 2018, *A&A*, **616**, A1
- Gazeas K. D., 2009, *Communications in Asteroseismology*, **159**, 129
- Gazeas K. D., Niarchos P. G., 2006, *MNRAS*, **372**, L83
- Gazeas K., Stępień K., 2008, *MNRAS*, **390**, 1577
- Gazeas K., et al., 2021a, *MNRAS*, **501**, 2897
- Gazeas K. D., et al., 2021b, *MNRAS*, **502**, 2879
- Harmanec P., 1988, *Bulletin of the Astronomical Institutes of Czechoslovakia*, **39**, 329
- Haroou A. A., Essam A., Basurah H., 2018, *Astrophysics*, **61**, 458
- Henden A. A., Templeton M., Terrell D., Smith T. C., Levine S., Welch D., 2016, VizieR Online Data Catalog, p. [II/336](https://vizier.cfa.harvard.edu/vizier/doc/II/336)
- Hilditch R. W., King D. J., McFarlane T. M., 1988, *MNRAS*, **231**, 341
- Jayasinghe T., et al., 2019, *MNRAS*, **486**, 1907
- Jiang D., Han Z., Ge H., Yang L., Li L., 2012, *MNRAS*, **421**, 2769
- Kirk B., et al., 2016, *AJ*, **151**, 68
- Kjurkchieva D. P., Dimitrov D. P., Ibryamov S. I., Vasileva D. L., 2018, *Publ. Astron. Soc. Australia*, **35**, e008
- Koen C., Koen T., Gray R. O., 2016, *AJ*, **151**, 168
- Koo J.-R., Lee J. W., Lee B.-C., Kim S.-L., Lee C.-U., Hong K., Lee D.-J., Rey S.-C., 2014, *AJ*, **147**, 104
- Kouzuma S., 2018, *PASJ*, **70**, 90
- Kreiner J. M., et al., 2003, *A&A*, **412**, 465
- Kubiak M., Udalski A., Szymanski M. K., 2006, *Acta Astron.*, **56**, 253
- Kwee K. K., van Woerden H., 1956, *Bull. Astron. Inst. Netherlands*, **12**, 327
- Lanza A. F., Rodonò M., 2002, *Astronomische Nachrichten*, **323**, 424
- Li L., Zhang F., 2006, *MNRAS*, **369**, 2001
- Li K., Xia Q.-Q., Michel R., Hu S.-M., Guo D.-F., Gao X., Chen X., Gao D.-Y., 2019, *MNRAS*, **485**, 4588
- Li K., Kim C.-H., Xia Q.-Q., Michel R., Hu S.-M., Gao X., Guo D.-F., Chen X., 2020, *AJ*, **159**, 189
- Liakos A., 2015, in Rucinski S. M., Torres G., Zejda M., eds, *Astronomical Society of the Pacific Conference Series Vol. 496, Living Together: Planets, Host Stars and Binaries*. p. 286
- Liu N. P., Qian S. B., Soonthornthum B., Zhu L. Y., Liao W. P., Zhao E. G., Zhou X., 2015, *AJ*, **149**, 148
- Lohr M. E., Norton A. J., Kolb U. C., Boyd D. R. S., 2013, *A&A*, **558**, A71
- Lohr M. E., Hodgkin S. T., Norton A. J., Kolb U. C., 2014, *A&A*, **563**, A34
- Lohr M. E., et al., 2015a, *A&A*, **578**, A103
- Lohr M. E., Norton A. J., Payne S. G., West R. G., Wheatley P. J., 2015b, *A&A*, **578**, A136
- Loukaidou G., Gazeas K., 2018, *Information Bulletin on Variable Stars*, **6237**, 1
- Lucy L. B., 1967, *Z. Astrophys.*, **65**, 89
- Maceroni C., Milano L., Russo G., 1982, *A&AS*, **49**, 123
- Michel R., Kjurkchieva D., 2019, *New Astron.*, **68**, 51
- Nefs S. V., et al., 2012, *MNRAS*, **425**, 950
- Norton A. J., et al., 2011, *A&A*, **528**, A90
- O'Connell D. J. K., 1951, *Publications of the Riverview College Observatory*, **2**, 100
- Paczynski B., Szczygieł D. M., Pilecki B., Pojmański G., 2006, *MNRAS*, **368**, 1311
- Pecaut M. J., Mamajek E. E., 2013, *ApJS*, **208**, 9
- Petrosky E., Hwang H.-C., Zakamska N. L., Chandra V., Hill M. J., 2021, *MNRAS*, **503**, 3975
- Pietrukowicz P., et al., 2017, *Acta Astron.*, **67**, 115
- Press W. H., Teukolsky S. A., Vetterling W. T., Flannery B. P., 1996, *Numerical Recipes in Fortran 90 (2nd Ed.): The Art of Parallel Scientific Computing*. Cambridge University Press, USA
- Pribulla T., Rucinski S. M., 2006, *AJ*, **131**, 2986
- Pribulla T., Kreiner J. M., Tremko J., 2003, *Contributions of the Astronomical Observatory Skalnaté Pleso*, **33**, 38
- Qian S., Zhu L., Liu L., Zhang X., Shi X., He J., Zhang J., 2020, *Research in Astronomy and Astrophysics*, **20**, 163
- Rasio F. A., 1995, *ApJ*, **444**, L41
- Ruciński S. M., 1969, *Acta Astron.*, **19**, 245
- Rucinski S. M., 1992, *AJ*, **103**, 960
- Rucinski S. M., 1993, in Sahade J., McCluskey G. E., Kondo Y., eds, *Astrophysics and Space Science Library Vol. 177, Astrophysics and Space Science Library*. p. 111, doi:[10.1007/978-94-011-2416-4_8](https://doi.org/10.1007/978-94-011-2416-4_8)
- Rucinski S. M., 2002, *PASP*, **114**, 1124
- Rucinski S. M., Pribulla T., van Kerkwijk M. H., 2007, *AJ*, **134**, 2353
- Rucinski S. M., Pribulla T., Budaj J., 2013, *AJ*, **146**, 70
- Saad M. S., Darwish M. S., Nasser M. A., Hamdy M. A., Beheary M. M., Gadallah K., Fouda D., 2016, *New Astron.*, **47**, 24
- Samus N. N., Durlevich O. V., Kazarovets E. V., Kireeva N. N., Pastukhova E. N., 2018, *Astronomy Reports*, **62**, 1050
- Schlaflly E. F., Finkbeiner D. P., 2011, *ApJ*, **737**, 103
- Soszyński I., et al., 2016, *Acta Astron.*, **66**, 405
- Stępień K., 2006, *Acta Astron.*, **56**, 347
- Stępień K., Gazeas K., 2012, *Acta Astron.*, **62**, 153
- Terrell D., Gross J., 2014, *Information Bulletin on Variable Stars*, **6104**, 1
- Terrell D., Wilson R. E., 2005, *Ap&SS*, **296**, 221
- Tokovinin A., Thomas S., Sterzik M., Udry S., 2006, *A&A*, **450**, 681
- Torres G., Andersen J., Giménez A., 2010, *A&ARv*, **18**, 67
- Tylenda R., et al., 2011, *A&A*, **528**, A114
- Tylenda R., et al., 2013, *A&A*, **555**, A16
- Watson C. L., Henden A. A., Price A., 2006, *Society for Astronomical Sciences Annual Symposium*, **25**, 47
- Wilson R. E., 1979, *ApJ*, **234**, 1054
- Wilson R. E., 1990, *ApJ*, **356**, 613
- Yakut K., Eggleton P. P., 2005, *ApJ*, **629**, 1055
- Zasche P., Liakos A., Niarchos P., Wolf M., Manimanis V., Gazeas K., 2009, *New Astron.*, **14**, 121
- Zasche P., et al., 2019, *A&A*, **630**, A128
- Zhang X.-D., Qian S.-B., 2020, *MNRAS*, **497**, 3493
- Zhang X. B., et al., 2014, *AJ*, **148**, 40
- Zola S., et al., 2004, *Acta Astron.*, **54**, 299
- de Jong J. T. A., Yanny B., Rix H.-W., Dolphin A. E., Martin N. F., Beers T. C., 2010, *ApJ*, **714**, 663
- peng Lu H., yun Zhang L., Michel R., Han X. L., 2020, *ApJ*, **901**, 169

Table A1. Results derived from light curve modeling.

Parameters	1SWASP	1SWASP	1SWASP	1SWASP	1SWASP
	J030749.87-365201.7	J040615.79-425002.3	J044132.96+440613.7	J050904.45-074144.4	J052926.88+461147.5
Fill-out factor	23 ± 5%	5 ± 2%	29 ± 7%	7 ± 6%	15 ± 3%
i [deg]	84.4 ± 0.9	72.6 ± 0.9	88.5 ± 0.7	82.9 ± 0.5	88.7 ± 0.8
T_1 [K]	4700*	4900*	5350*	5000*	5400*
T_2 [K]	4578 ± 67	4559 ± 75	5056 ± 26	4985 ± 19	5328 ± 13
$\Omega_1=\Omega_2$	2.904 ± 0.017	4.546 ± 0.053	4.408 ± 0.039	2.507 ± 0.012	2.613 ± 0.007
q_{ph}	0.555 ± 0.066	1.532 ± 0.037	1.535 ± 0.022	0.325 ± 0.007	0.385 ± 0.003
L_1 (B)	7.873 ± 0.039	5.975 ± 0.063	5.557 ± 0.035	8.560 ± 0.048	8.411 ± 0.038
L_1 (V)	7.891 ± 0.038	5.884 ± 0.061	5.418 ± 0.048	8.653 ± 0.046	8.444 ± 0.034
L_1 (R)	8.002 ± 0.038	5.803 ± 0.060	5.292 ± 0.043	8.718 ± 0.045	8.517 ± 0.033
L_1 (I)	7.864 ± 0.037	5.641 ± 0.058	5.040 ± 0.028	8.831 ± 0.044	8.462 ± 0.029
L_2 (B)	3.937 ^a	5.599 ^a	5.887 ^a	3.031 ^a	3.309 ^a
L_2 (V)	4.010 ^a	5.744 ^a	5.977 ^a	3.067 ^a	3.351 ^a
L_2 (R)	4.128 ^a	5.892 ^a	6.029 ^a	3.093 ^a	3.405 ^a
L_2 (I)	4.168 ^a	6.161 ^a	6.044 ^a	3.141 ^a	3.422 ^a
l_3 (B)	0	0	0.006 ± 0.004	0	0
l_3 (V)	0	0	0.028 ± 0.008	0	0
l_3 (R)	0	0	0.041 ± 0.008	0	0
l_3 (I)	0	0	0.069 ± 0.006	0	0
r_1 ^{side}	0.4460	0.4177	0.4362	0.4859	0.4740
r_2 ^{side}	0.3374	0.3391	0.3569	0.2818	0.2995
co-latitude	164.4 ± 1.4	91.6 ± 9.1	120.5 ± 10.4	162.4 ± 2.2	122.9 ± 9.7
longitude	47.4 ± 1.9	174.6 ± 3.7	131.2 ± 5.6	49.3 ± 3.7	121.7 ± 4.3
radius	49.2 ± 0.9	21.1 ± 3.8	16.3 ± 2.6	42.2 ± 2.2	14.5 ± 3.0
temp. factor	0.163 ± 0.031	0.828 ± 0.071	0.757 ± 0.064	0.702 ± 0.064	0.763 ± 0.090

(*): Fixed parameter, (a): Calculated according to L_1 **Table A2.** Results derived from light curve modeling (continued).

Parameters	1SWASP	1SWASP	1SWASP	1SWASP	1SWASP
	J055416.98+442534.0	J080150.03+471433.8	J092328.76+435044.8	J092754.99-391053.4	J093010.78+533859.5
Fill-out factor	11 ± 10%	9 ± 8%	20 ± 9%	12 ± 5%	19 ± 2%
i [deg]	75.4 ± 0.6	86.3 ± 1.2	83.2 ± 0.7	72.1 ± 1.9	88.0 ± 1.3
T_1 [K]	5250*	4650*	5800*	5400*	4700*
T_2 [K]	5266 ± 37	4720 ± 12	5788 ± 32	5172 ± 11	4800 ± 36
$\Omega_1=\Omega_2$	2.288 ± 0.015	2.755 ± 0.023	2.646 ± 0.022	2.862 ± 0.016	2.627 ± 0.004
q_{ph}	0.229 ± 0.010	0.451 ± 0.012	0.409 ± 0.011	0.511 ± 0.074	0.397**
L_1 (U)	–	–	–	7.972 ± 0.053	–
L_1 (B)	9.318 ± 0.104	7.565 ± 0.141	8.245 ± 0.089	8.130 ± 0.056	2.384 ± 0.043
L_1 (V)	9.521 ± 0.099	7.644 ± 0.149	8.256 ± 0.083	8.186 ± 0.055	2.479 ± 0.043
L_1 (R)	9.524 ± 0.096	7.474 ± 0.157	8.207 ± 0.079	8.150 ± 0.052	2.556 ± 0.044
L_1 (I)	9.629 ± 0.093	7.546 ± 0.155	8.170 ± 0.071	–	2.661 ± 0.046
L_2 (U)	–	–	–	3.435 ^a	–
L_2 (B)	2.512 ^a	4.036 ^a	3.664 ^a	3.490 ^a	1.169 ^a
L_2 (V)	2.560 ^a	4.043 ^a	3.674 ^a	3.620 ^a	1.203 ^a
L_2 (R)	2.555 ^a	3.920 ^a	3.656 ^a	3.692 ^a	1.225 ^a
L_2 (I)	2.575 ^a	3.897 ^a	3.644 ^a	–	1.249 ^a
l_3 (U)	–	–	–	0	–
l_3 (B)	0	0.005 ± 0.010	0	0	0.702 ± 0.045
l_3 (V)	0	0.005 ± 0.011	0	0	0.694 ± 0.046
l_3 (R)	0	0.040 ± 0.012	0	0	0.685 ± 0.047
l_3 (I)	0	0.037 ± 0.012	0	–	0.676 ± 0.049
r_1 ^{side}	0.5215	0.4557	0.4717	0.4454	0.4736
r_2 ^{side}	0.2566	0.3097	0.3077	0.3221	0.3044
co-latitude	157.0 ± 10.5	–	150.7 ± 3.0	–	92.1 ± 1.3
longitude	265.2 ± 5.5	–	115.7 ± 2.6	–	72.1 ± 0.5
radius	24.0 ± 5.1	–	20.2 ± 5.7	–	19.7 ± 0.2
temp. factor	0.208 ± 0.051	–	0.360 ± 0.084	–	0.846 ± 0.001

(*): Fixed parameter, (**): Fixed mass ratio from spectroscopy (Lohr et al. 2015a), (a): Calculated according to L_1

Table A3. Results derived from light curve modeling (continued).

Parameters	1SWASP	1SWASP	1SWASP	1SWASP	2MASS
	J114929.22-423049.0	J121906.35-240056.9	J133105.91+121538.0	J150822.80-054236.9	J15165453+0048263
Fill-out factor	16 ± 5%	10 ± 9%	18 ± 8%	11 ± 9%	29 ± 4%
i [deg]	79.6 ± 0.2	73.0 ± 1.2	75.0 ± 0.1	86.8 ± 0.5	63.7 ± 0.9
T_1 [K]	4150*	4650*	5150*	5150*	6150*
T_2 [K]	4075 ± 34	4335 ± 99	4845 ± 15	5130 ± 16	6095 ± 71
$\Omega_1=\Omega_2$	2.525 ± 0.010	5.835 ± 0.255	5.032 ± 0.069	2.860 ± 0.029	2.933 ± 0.010
q_{ph}	0.343 ± 0.049	2.465 ± 0.283	1.923 ± 0.051	0.510**	0.584 ± 0.051
L_1 (U)	–	–	–	–	6.902 ± 0.422
L_1 (B)	8.861 ± 0.035	5.039 ± 0.065	5.136 ± 0.064	7.807 ± 0.089	6.998 ± 0.305
L_1 (V)	8.853 ± 0.033	4.894 ± 0.065	5.071 ± 0.064	7.664 ± 0.095	7.096 ± 0.300
L_1 (R)	8.871 ± 0.032	4.711 ± 0.067	4.975 ± 0.064	7.686 ± 0.100	7.072 ± 0.293
L_1 (I)	8.782 ± 0.032	4.533 ± 0.063	4.850 ± 0.064	7.766 ± 0.098	–
L_2 (U)	–	–	–	–	4.085 ^a
L_2 (B)	2.821 ^a	6.858 ^a	6.432 ^a	4.152 ^a	4.177 ^a
L_2 (V)	2.970 ^a	7.089 ^a	6.602 ^a	4.085 ^a	4.258 ^a
L_2 (R)	3.075 ^a	7.179 ^a	6.700 ^a	4.106 ^a	4.265 ^a
L_2 (I)	3.117 ^a	7.476 ^a	6.919 ^a	4.163 ^a	–
l_3 (U)	–	–	–	–	0
l_3 (B)	0	0	0	0.005 ± 0.001	0
l_3 (V)	0	0	0	0.011 ± 0.004	0
l_3 (R)	0	0	0	0.016 ± 0.007	0
l_3 (I)	0	0	0	0.010 ± 0.007	–
r_1 ^{side}	0.4860	0.4664	0.4485	0.4455	0.4458
r_2 ^{side}	0.2909	0.3014	0.3281	0.3217	0.3468
co-latitude	–	164.2 ± 9.5	–	171.5 ± 1.2	136.0 ± 2.4
longitude	–	206.2 ± 3.6	–	39.1 ± 4.6	230.7 ± 1.7
radius	–	72.5 ± 3.7	–	40.4 ± 1.5	13.2 ± 1.3
temp. factor	–	0.861 ± 0.017	–	0.572 ± 0.044	0.653 ± 0.087

(*): Fixed parameter, (**): Fixed mass ratio from spectroscopy (Lohr et al. 2014), (a): Calculated according to L_1

Table A4. Results derived from light curve modeling (continued).

Parameters	1SWASP	1SWASP	1SWASP	1SWASP	1SWASP
	J1161335.80-284722.2	J170240.07+151123.5	J173003.21+344509.4	J173828.46+111150.2	J174310.98+432709.6
Fill-out factor	13 ± 7%	14 ± 3%	13 ± 7%	1 ± 2%	13 ± 9%
i [deg]	78.3 ± 1.5	89.4 ± 0.4	67.7 ± 0.7	67.9 ± 0.7	77.2 ± 0.6
T_1 [K]	4550*	5000*	4700*	5250*	5300*
T_2 [K]	4347 ± 40	5307 ± 17	4475 ± 18	5065 ± 21	4996 ± 18
$\Omega_1=\Omega_2$	4.402 ± 0.039	2.537 ± 0.007	3.120 ± 0.026	2.431 ± 0.004	2.990 ± 0.031
q_{ph}	1.468 ± 0.281	0.346 ± 0.003	0.658 ± 0.033	0.280 ± 0.001	0.584 ± 0.036
L_1 (B)	5.729 ± 0.373	7.474 ± 0.036	7.618 ± 0.241	9.303 ± 0.052	8.192 ± 0.152
L_1 (V)	5.619 ± 0.370	7.763 ± 0.035	6.596 ± 0.239	9.393 ± 0.043	7.907 ± 0.159
L_1 (R)	5.438 ± 0.350	7.975 ± 0.061	6.525 ± 0.238	9.508 ± 0.039	7.818 ± 0.159
L_1 (I)	5.224 ± 0.337	8.133 ± 0.055	6.086 ± 0.231	9.535 ± 0.029	7.408 ± 0.149
L_2 (B)	5.747 ^a	4.035 ^a	3.756 ^a	2.339 ^a	3.597 ^a
L_2 (V)	5.895 ^a	4.013 ^a	3.364 ^a	2.422 ^a	3.620 ^a
L_2 (R)	5.911 ^a	3.982 ^a	3.429 ^a	2.503 ^a	3.703 ^a
L_2 (I)	5.986 ^a	3.845 ^a	3.368 ^a	2.593 ^a	3.703 ^a
l_3 (B)	0.000 ± 0.002	0	0.006 ± 0.001	0	0.000 ± 0.001
l_3 (V)	0.012 ± 0.002	0	0.122 ± 0.027	0	0.021 ± 0.012
l_3 (R)	0.023 ± 0.003	0	0.132 ± 0.027	0	0.040 ± 0.012
l_3 (I)	0.041 ± 0.003	0	0.182 ± 0.026	0	0.069 ± 0.009
r_1 ^{side}	0.4199	0.4835	0.4227	0.4943	0.4337
r_2 ^{side}	0.3489	0.2902	0.3455	0.2646	0.3346
co-latitude	–	–	121.2 ± 10.9	127.8 ± 6.4	172.3 ± 2.7
longitude	–	–	281.6 ± 6.5	254.5 ± 3.1	318.1 ± 6.6
radius	–	–	23.4 ± 6.5	16.5 ± 0.3	53.6 ± 2.6
temp. factor	–	–	0.838 ± 0.057	0.704 ± 0.023	0.738 ± 0.068

(*): Fixed parameter, (a): Calculated according to L_1

Table A5. Results derived from light curve modeling (continued).

Parameters	1SWASP	1SWASP	2MASS	2MASS	1SWASP
	J180947.64+490255.0	J195900.31-252723.1	J21031997+0209339	J21042404+0731381	J212454.61+203030.8
Fill-out factor	16 ± 5%	18 ± 5%	13 ± 4%	3 ± 2%	5 ± 5%
i [deg]	82.3 ± 0.2	88.9 ± 2.3	82.4 ± 0.5	78.9 ± 0.7	89.0 ± 2.1
T_1 [K]	4050*	5400*	4400*	4800*	5250*
T_2 [K]	3833 ± 24	5244 ± 96	4179 ± 20	4772 ± 24	5264 ± 70
$\Omega_1=\Omega_2$	3.614 ± 0.027	4.915 ± 0.031	3.666 ± 0.020	2.471 ± 0.003	2.721 ± 0.014
q_{ph}	0.967 ± 0.016	1.836 ± 0.022	0.992 ± 0.011	0.306 ± 0.041	0.428 ± 0.007
L_1 (B)	7.940 ± 0.039	4.557 ± 0.037	6.939 ± 0.037	8.886 ± 0.139	8.167 ± 0.406
L_1 (V)	6.940 ± 0.042	4.666 ± 0.036	6.770 ± 0.036	8.475 ± 0.189	8.049 ± 0.409
L_1 (R)	6.481 ± 0.043	4.581 ± 0.034	6.696 ± 0.035	8.154 ± 0.179	7.992 ± 0.406
L_1 (I)	6.395 ± 0.044	4.573 ± 0.031	6.591 ± 0.034	7.764 ± 0.139	8.082 ± 0.421
L_2 (B)	3.531 ^a	6.693 ^a	4.492 ^a	2.921 ^a	3.812 ^a
L_2 (V)	4.575 ^a	6.994 ^a	4.684 ^a	2.788 ^a	3.749 ^a
L_2 (R)	5.077 ^a	6.981 ^a	4.864 ^a	2.694 ^a	3.716 ^a
L_2 (I)	5.383 ^a	7.151 ^a	5.104 ^a	2.573 ^a	3.748 ^a
l_3 (B)	0	0.035 ± 0.001	0	0.009 ± 0.008	0.001 ± 0.001
l_3 (V)	0	0.041 ± 0.002	0	0.061 ± 0.014	0.017 ± 0.002
l_3 (R)	0	0.046 ± 0.003	0	0.098 ± 0.014	0.036 ± 0.002
l_3 (I)	0	0.046 ± 0.003	0	0.141 ± 0.008	0.030 ± 0.002
r_1 ^{side}	0.3901	0.4436	0.3858	0.4899	0.4581
r_2 ^{side}	0.3839	0.3316	0.3844	0.2743	0.3027
co-latitude	–	–	–	136.9 ± 10.2	88.8 ± 9.6
longitude	–	–	–	16.6 ± 4.4	354.9 ± 0.7
radius	–	–	–	26.6 ± 5.9	40.0 ± 0.7
temp. factor	–	–	–	0.672 ± 0.098	0.963 ± 0.015

(*): Fixed parameter, (a): Calculated according to L_1 **Table A6.** Results derived from light curve modeling (continued).

Parameters	1SWASP	1SWASP	1SWASP	1SWASP	1SWASP
	J212808.86+151622.0	J220734.47+265528.6	J221058.82+251123.4	J224747.20-351849.3	J232610.13-294146.6
Fill-out factor	16 ± 8%	0 ± 1%	17 ± 10%	0 ± 5%	8 ± 7%
i [deg]	75.4 ± 0.3	70.5 ± 0.2	78.8 ± 0.2	58.4 ± 1.1	75.9 ± 0.9
T_1 [K]	4700*	4900*	4950*	4300*	4850*
T_2 [K]	4342 ± 48	4862 ± 20	4662 ± 28	3884 ± 33	4496 ± 72
$\Omega_1=\Omega_2$	5.305 ± 0.061	4.574 ± 0.003	5.532 ± 0.059	3.344 ± 0.020	6.519 ± 0.052
q_{ph}	2.108 ± 0.047	1.508 ± 0.004	2.276 ± 0.045	0.697 ± 0.013	2.965 ± 0.037
L_1 (B)	5.258 ± 0.091	4.868 ± 0.040	4.728 ± 0.050	9.648 ± 0.065	4.714 ± 0.052
L_1 (V)	4.893 ± 0.084	4.902 ± 0.036	4.578 ± 0.050	8.700 ± 0.059	4.617 ± 0.051
L_1 (R)	4.728 ± 0.083	4.922 ± 0.033	4.420 ± 0.050	8.151 ± 0.058	4.477 ± 0.050
L_1 (I)	4.519 ± 0.047	4.884 ± 0.027	4.029 ± 0.048	7.845 ± 0.056	4.219 ± 0.047
L_2 (B)	5.833 ^a	6.833 ^a	6.816 ^a	2.010 ^a	7.742 ^a
L_2 (V)	5.803 ^a	6.905 ^a	6.818 ^a	2.966 ^a	7.946 ^a
L_2 (R)	5.927 ^a	6.962 ^a	6.796 ^a	3.526 ^a	8.045 ^a
L_2 (I)	6.186 ^a	6.959 ^a	6.575 ^a	3.874 ^a	8.199 ^a
l_3 (B)	0.042 ± 0.009	0	0.003 ± 0.003	0	0
l_3 (V)	0.074 ± 0.008	0	0.035 ± 0.003	0	0
l_3 (R)	0.084 ± 0.008	0	0.056 ± 0.003	0	0
l_3 (I)	0.081 ± 0.008	0	0.113 ± 0.003	0	0
r_1 ^{side}	0.4556	0.4084	0.4634	0.3995	0.483
r_2 ^{side}	0.3186	0.3329	0.3125	0.3475	0.2852
co-latitude	137.1 ± 2.3	–	170.3 ± 0.6	–	166.1 ± 6.2
longitude	155.4 ± 1.4	–	50.5 ± 1.7	–	219.3 ± 7.4
radius	35.7 ± 1.7	–	49.3 ± 0.2	–	86.6 ± 7.9
temp. factor	0.853 ± 0.004	–	0.643 ± 0.021	–	0.813 ± 0.099

(*): Fixed parameter, (a): Calculated according to L_1 **APPENDIX A: MODELING RESULTS**This paper has been typeset from a $\text{\TeX}/\text{\LaTeX}$ file prepared by the author.